Atmospheric Research 215 (2019) 253–267

Contents lists available at ScienceDirect

Atmospheric Research

journal homepage: www.elsevier.com/locate/atmosres

Sensitivity of WRF simulations with the YSU PBL scheme to the lowest model level height for a sea fog event over the Yellow Sea

Yue Yang[a], Xiao-Ming Hu[b,c], Shanhong Gao[a,*], Yongming Wang[d]

[a] Key Laboratory of Physical Oceanography, College of Oceanic and Atmospheric Sciences, Ocean University of China, Qingdao 266100, China
[b] Key Laboratory for Aerosol-Cloud-Precipitation of China Meteorological Administration, Nanjing University of Information Science & Technology, Nanjing 210044, China
[c] Center for Analysis and Prediction of Storms and School of Meteorology, University of Oklahoma, Norman, OK 73072, USA
[d] School of Meteorology, University of Oklahoma, Norman, OK 73072, USA

ARTICLE INFO

Keywords:
Lowest model level height
WRF
YSU PBL scheme
Sea fog
Virtual potential temperature at z_1

ABSTRACT

The lowest model level is the interface of energy and mass exchanging between the surface and planetary boundary layer (PBL). Previous studies mostly examined the role of the lowest model level height (z_1) in simulating the continental PBL processes. The impact of z_1 on simulating marine processes (e.g., sea fog), however, remains unclear. The present study explores the sensitivity of the Weather Research and Forecasting (WRF) model with the Yonsei University (YSU) PBL scheme to z_1 for an advection fog event occurred on 27 March 2012 over the Yellow Sea. Seven experiments with various z_1 (28, 22, 14, 8, 4, 1 and 0.4 m) are conducted.

Evaluations for the continental PBL indicate that z_1 below 8 m is irrational in simulating surface temperature and PBL height over land. However, the model with $z_1 =$ 8 m gives the best performance in terms of reproducing sea fog. When z_1 gets below 8 m, the sea fog occurs too early and the fog area is too small. As z_1 exceeds 8 m, the fog forms too late and the fog area becomes underestimated. These model sensitivities can be explained by the impact of z_1 on virtual potential temperature at z_1 [$\theta_v(z_1)$]. Since the heat capacity of the air in the lowest model layer is proportional to z_1, a lower (higher) z_1 causes a quicker (slower) response of $\theta_v(z_1)$ to surface cooling, thus leading to an earlier (later) sea fog formation. After the fog onset, especially for a lower z_1, the variation of $\theta_v(z_1)$ is dominated by turbulent heating that transports warmer air above to the very shallow lowest model layer, resulting in a lower vertical growth and even earlier dissipation of the sea fog.

1. Introduction

Sea fog occurs within the marine atmospheric boundary layer. It can significantly reduce the atmospheric horizontal visibility and pose a severe risk/damage to many human activities (e.g., aviation, shipping, and social economy) in both coastal and marine regions (Gultepe et al., 2007; Koračin and Dorman, 2017; Trémant, 1987). Sea fog can be mainly categorized into advection fog and steam fog (Heo et al., 2010; Wang, 1985). Advection fog is the primary sea fog type over the Yellow Sea (YS; its location is shown in Fig. 1), which usually forms when the warm and moist air mass above the Kuroshio Current moves northward to a cold sea surface (Gao et al., 2007; Koračin et al., 2014; Zhang et al., 2015) under an appropriate synoptic system, such as rear of transition high to sea (Gao et al., 2007; Wang, 1985; Yang and Gao, 2015). Based on long-term observations, Wang (1985) specified the lower boundary conditions favorable for the occurrence of advection fog, such as the maximum of sea surface temperature ($SST \leq 25\,^{\circ}C$), the temperature difference between air and sea (0.5–3.0 °C), and the wind speed (1.6–10.8 m s^{-1}). The formation of advection fog is a process of diabatic phase transition within the planetary boundary layer (PBL) (Gao et al., 2007; Gultepe et al., 2007). Turbulent mixing (Gao et al., 2007; Lamb, 1943; Taylor, 1917) and radiation (Findlater et al., 1989; Koračin et al., 2001; Oliver et al., 1978) play important roles in cooling and moistening the air during the sea fog occurrence. However, open questions still remain about the mechanisms/processes that contribute to sea fog formation and evolution, for instance, the air-sea interaction (e.g., Koračin and Dorman, 2017; Zhang, 2012; Zhang et al., 2009).

The methodology to study sea fog over the YS has been evolving in the past years. Traditional studies primarily focus on climatological and synoptic characteristics using observations and reanalysis datasets (Cho et al., 2000; Kim and Yum, 2010; Wang, 1985; Zhang et al., 2015). With the rapid growth of computation capability of supercomputers recently,

* Corresponding author at: Key Laboratory of Physical Oceanography, College of Oceanic and Atmospheric Sciences, Ocean University of China, 5 Yushan Road, Qingdao 266003, China.
E-mail address: gaosh@ouc.edu.cn (S. Gao).

https://doi.org/10.1016/j.atmosres.2018.09.004
Received 2 December 2017; Received in revised form 29 May 2018; Accepted 5 September 2018
Available online 13 September 2018

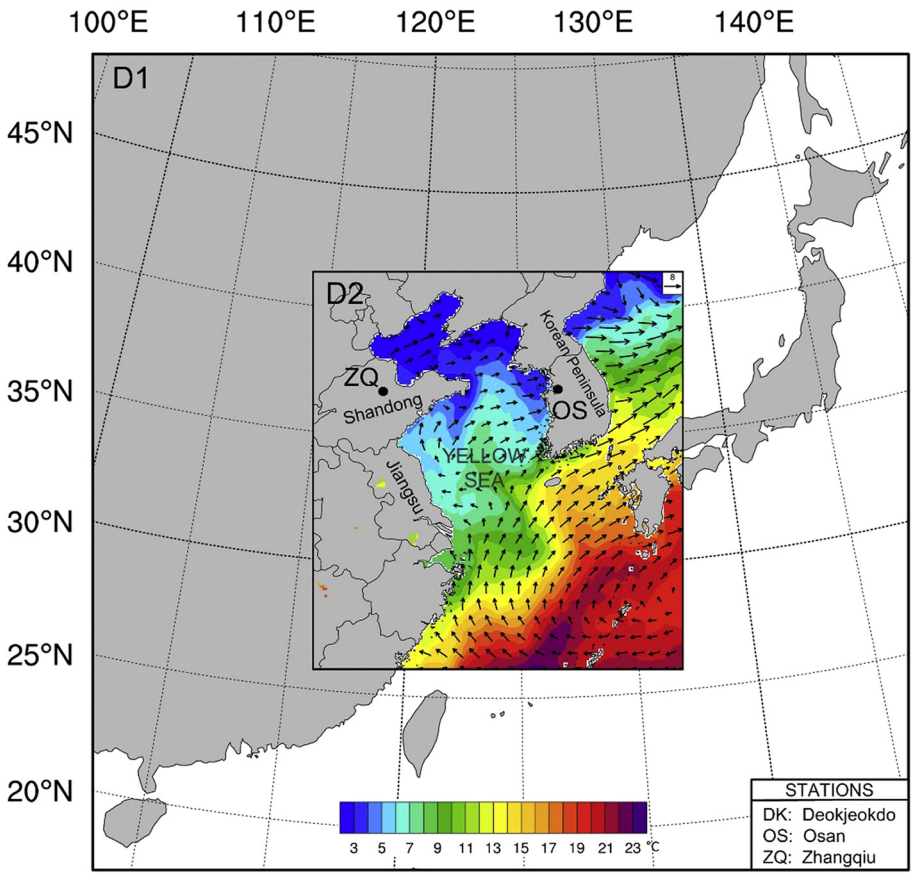

Fig. 1. Geographic map of the Yellow Sea and two nesting domains used for WRF simulations. Distributions of sea surface temperature[1] (*SST*, colour shaded in D2) and modeled 10-m wind field (vectors) at 2100 LST (=UTC + 8 h) 27 March 2012 in D2. Locations of named radiosonde stations (black dots) are marked. (For interpretation of the references to colour in this figure legend, the reader is referred to the web version of this article.)

high-resolution three-dimensional (3D) numerical simulations with different physics parameterizations have been increasingly used to investigate various mechanisms for sea fog formation and evolution (Fu et al., 2006, 2012; Gao et al., 2007; Kim and Yum, 2012; Wang et al., 2014). The 3D model simulations of sea fog show a large sensitivity to initial atmospheric conditions (Bergot and Guedalia, 1994; Bergot et al., 2007; Gao et al., 2007, 2010; Koračin and Dorman, 2017; Koračin et al., 2005b, 2014; Lewis et al., 2004; Pagowski et al., 2004). With appropriate initial conditions, the PBL scheme (e.g., Avolio et al., 2017; Braun and Tao, 2000; Chaouch et al., 2017; Cohen et al., 2015; Coniglio et al., 2013; García-Díez et al., 2013; Han et al., 2008; Hariprasad et al., 2014; Hu et al., 2010, 2013; Huang et al., 2013; Nolan et al., 2009; Román-Cascón et al., 2012; Shin and Hong, 2011; Wang et al., 2014; Zhang and Pu, 2017) and microphysics (MP) scheme (e.g., Borge et al., 2008; Jankov et al., 2005, 2007; Khain et al., 2016; Li and Pu, 2008; Van der Velde et al., 2010) are found to play major roles in capturing the processes of turbulent mixing and phase changes of hydrometeors during the lifetime of sea fog. In their simulations of 10 sea fog cases over the YS using the Weather Research and Forecasting (WRF) model (Skamarock et al., 2008) with various PBL and MP schemes, Lu et al. (2014) found that compared to MP schemes, sea fog formation and evolution are more sensitive to PBL schemes, among which the Yonsei University (YSU; Hong, 2010; Hong et al., 2006) and the Mellor-Yamada-Nakanishi-Niino (MYNN; Nakanishi and Niino, 2006, 2009) schemes are more skillful. In their forecasts of 2 radiation fog events over a flat terrain area in the Netherlands, Steeneveld et al. (2015) reported that the YSU scheme performs better than the MYNN scheme with more accurate timing of onset, more widespread fog area and higher liquid water content (*LWC*). However, even though these physics schemes show reasonably good skills in reproducing fog processes, their performances rely heavily on the model resolution, particularly the vertical resolution (e.g., Bechtold et al., 1996; Bergot and Guedalia, 1994; Bergot et al., 2007; Kong, 2002; Koračin and Dorman, 2017; Koračin et al., 2005b, 2014; Lewis et al., 2004; Steeneveld et al., 2015; Tardif, 2007; Van der Velde et al., 2010).

Previous studies have illustrated a strong dependence of model performance on vertical resolution for various atmospheric phenomena/processes, such as hurricanes (Kimball and Dougherty, 2006; Zhang and Wang, 2003), rainfall (Aligo et al., 2009) and dust events (Teixeira et al., 2016). However, few studies have examined the sensitivity of sea fog simulations to vertical resolution. Gao et al. (2007) argued that an adequately fine resolution (particularly vertical resolution in the PBL) is required to capture the major characteristics of sea fog over the YS based on their simulations using the fifth-generation Mesoscale Model (MM5). Yang and Gao (2016) reported that the WRF simulation of a shallow sea fog over the YS was improved by enhancing vertical resolution within the PBL. The improvement is attributed to better resolving of *LWC* atop the fog layer with finer vertical resolution. However, advection fog over the YS always forms near the cold sea surface initially, which makes the vertical resolution at the bottom of the PBL a critical factor for the advection fog simulation.

In addition, the advection fog simulation also shows significant sensitivities to the treatments of the lower boundary conditions. Sensitivity experiments of tuning *SST* conducted by Gao et al. (2007) and Zhang and Ren (2010) proved that stability and turbulence below 100 m are sensitive to the variations of *SST*, leading to changes of sea fog area. Due to the significant improvement of wind structure, Wang and Gao (2016) gained a better coastal sea fog simulation by assimilating Doppler coastal radar radial velocity data. Compared to the studies on these lower boundary conditions, little attention has been paid to the influence of high vertical resolution at the bottom of the PBL on the simulation of sea fog formation and evolution.

The lowest model level, as one part of vertical resolution configuration at the bottom, plays the most vital role in vertically resolving the near-surface and PBL processes. For simulations of the PBL over land, the surface layer scheme calculates surface momentum flux and

Table 1
Summary of previous studies in the literature on the lowest model level height z_1.

z_1 (m)	Model	Phenomenon	Condition	Surface	Optimal/Critical value
40, 10, 3	MM5	Snowmelt	Stable	Land	10 m or less
36, 22, 7	MM5	Foehn	Stable	Land	Closer to the ground for wind; 22 m for temperature
27, 13	WRF	Cold pool	Stable	Land	13 m
54, 10	WRF	Rainfall	Convective	Land	below 10 m
90, 64, 40, 24, 16, 12, 8, 6, 4	WRF	Diurnal cycle	Stable and unstable	Land	12 m in daytime; 40 m at night
20, 12, 8, 6, 4	WRF	Tropical cyclone	Convective	Sea	below 12 m

exchange coefficients using the lowest model level height (z_1) and variables at z_1 based on the Monin-Obukhov similarity (Foken, 2006; Monin and Obukhov, 1954), and these coefficients enable surface heat and moisture fluxes to be calculated by the land surface model (LSM) (Skamarock et al., 2008). These surface fluxes then act as lower boundary conditions for turbulent exchange within the PBL (Koračin and Dorman, 2017; Shin et al., 2012). Most previous work examining the critical role of z_1 focused on phenomena/processes in the continental PBL, for instance, snowmelt (Wei et al., 2001), foehn (Zängl et al., 2008), cold pool (Wilson and Fovell, 2016) and rainfall (Aligo et al., 2009). Model configurations and optimal/critical z_1 determined for simulating these atmospheric phenomena/processes are summarized in Table 1. In these studies, the MM5 and WRF models were employed to explore the sensitivity of simulations to z_1 with the value of z_1 varying from 3 m for a very stable thermal stratification to 90 m for a highly unstable condition over land.

In contrast to the treatment for the continental PBL, surface fluxes of momentum, heat, and moisture all are calculated in the surface layer scheme for the marine PBL. Our knowledge regarding how different configurations of z_1 would affect simulations of the marine PBL is still limited. Sea fog simulations may be more sensitive to the selection of z_1 than simulations over land because of the generally lower marine PBL height, which typically ranges from a few tens of meters to several hundreds of meters (e.g., Hennemuth and Lammert, 2006; Subrahamanyam et al., 2012). In models, surface fluxes are calculated in the lowest model level using the similarity theory, which is only valid in the surface layer (normally defined as the bottom 5% to 10% of the PBL; Stull, 1988). Thus, theoretically, the optimal z_1 should be located within the surface layer. Since the PBL (and also the surface layer) over the ocean is typically shallower than that over the continent under the same stratification, optimal z_1 for simulating the marine PBL should also be lower than that for the continental PBL. Generally, z_1 was set to range from 28 to 4 m in previous numerical studies of sea fog over the YS (e.g., Choi and Speer, 2006; Fu et al., 2006; Gao et al., 2007, 2010; Kim and Yum, 2012; Lu et al., 2014; Wang et al., 2014; Yang and Gao, 2016; Zhang et al., 2008). A "too high" z_1 is speculated to lead to a relatively low skill in modeling fog onset (Gultepe et al., 2007; Román-Cascón et al., 2012; Steeneveld et al., 2015; Zhou et al., 2011). Therefore, a relatively low z_1 is necessary for sea fog simulation, and its lower limit still needs to be reasonably determined.

The YSU PBL scheme is employed in the present study for its good skill in capturing fog processes (Lu et al., 2014; Steeneveld et al., 2015). This first-order closure scheme uses the *K*-profile approach to parameterize turbulent mixing, and includes a countergradient nonlocal term and an explicit entrainment term in the turbulence flux equation (Hong, 2010; Hong et al., 2006; Noh et al., 2003). The WRF model with the YSU PBL scheme has been widely applied for various applications (e.g., meteorology, wind energy, and air quality) and approved to be able to realistically capture the PBL structure (e.g., Hu et al., 2013). Shin et al. (2012) demonstrated that the YSU scheme in the WRF model is sensitive to z_1 for the continental PBL in a one-day case study. They modified the YSU scheme (since WRF version 3.3.1) to make it work with a thinner surface layer by mitigating this drastic sensitivity. Ma et al. (2014) further examined the sensitivity of the modified YSU scheme to z_1 for a tropical cyclone case. Advection fog over the YS normally develops in stable marine PBL. Under such kind of stable condition, the sensitivity of this updated YSU scheme to z_1 remains unclear, and its impacts on the simulation of sea fog formation and evolution need further investigation.

A typical advection fog event over the YS on 27 March 2012 is investigated in the present study using observations and simulations of the Advanced Research WRF (ARW) model (version 3.8.1) with the YSU PBL scheme. The role of z_1 in reproducing this sea fog event and the sensitivity of model simulation to z_1 are examined. The rest of the manuscript is organized as follows. A brief review of the sea fog case and the numerical experiment design are introduced in Section 2. Data and methods used for evaluating the simulated results are also described in this section. Section 3 discusses model results in detail, including verifications for the rationality of z_1 and diagnostics analysis of the sensitivity of sea fog simulations to z_1. Conclusions and discussion are presented in Section 4.

2. Numerical experiments and evaluation methods

2.1. Sea fog case

A sea fog event over the YS that initiated on 27 March 2012 and dissipated on 29 March 2012 is selected for this study. The MODerate-resolution Imaging Spectroradiometer (MODIS) visible cloud image at 1300 local standard time (LST; LST = UTC + 8 h) 28 March captured this sea fog event (Fig. 2a). The fog was widespread, covering a large area from the northeastern to southwestern YS. The fog-top height was diagnosed from the Cloud-Aerosol Lidar and Infrared Pathfinder Satellite Observations (CALIPSO) data (Fig. 2b) (Liu et al., 2014; Minnis et al., 2008; Stein et al., 2011; Yi et al., 2015). The average fog-top height was ~150 m to the north of 35 ° N (red dashed line in Fig. 2a), while the fog was relatively shallow to the south of 35 ° N with an average fog-top height of ~60 m. The difference in the fog-top height was also manifested in the MODIS cloud image, which showed thick fog patch in bright white and shallow fog patch in light grey.

The MODIS aboard polar orbiting satellites (Terra and Aqua) is unable to capture detailed temporal variation of the sea fog event. The Multifunctional Transport Satellite (MTSAT) hourly data were adopted by Wang et al. (2014) to diagnose sea fog properties, and hourly variation of sea fog area and fog-top height are obtained (Fig. 3). According to the MTSAT data for the case in the present study, the shallow sea fog patch initially formed after 2000 LST 27 March (Fig. 3a, b) over the cold water when southwesterly winds and accompanied warm advection prevailed towards the southern tip of the Korean peninsula (*SST* and wind field in Fig. 1), which indicates this is a typical advection fog. At 0800 LST 28 March, the shallow fog patch spread westward (Fig. 3c) when the winds turned into southeasterly. However, the thick sea fog patch formed by a stratus-lowering process. From 2000 LST 27 March to 0200 LST 28 March, the satellite-derived sea fog covered the location of Deokjeokdo buoy at a height of ~200 m (Fig. 3a, b), but in fact there was no sea fog observed at the buoy (see measurements shown in

[1] The SST data is provided daily from North-East Asian Regional Global Ocean Observing System (NEAR-GOOS) dataset.

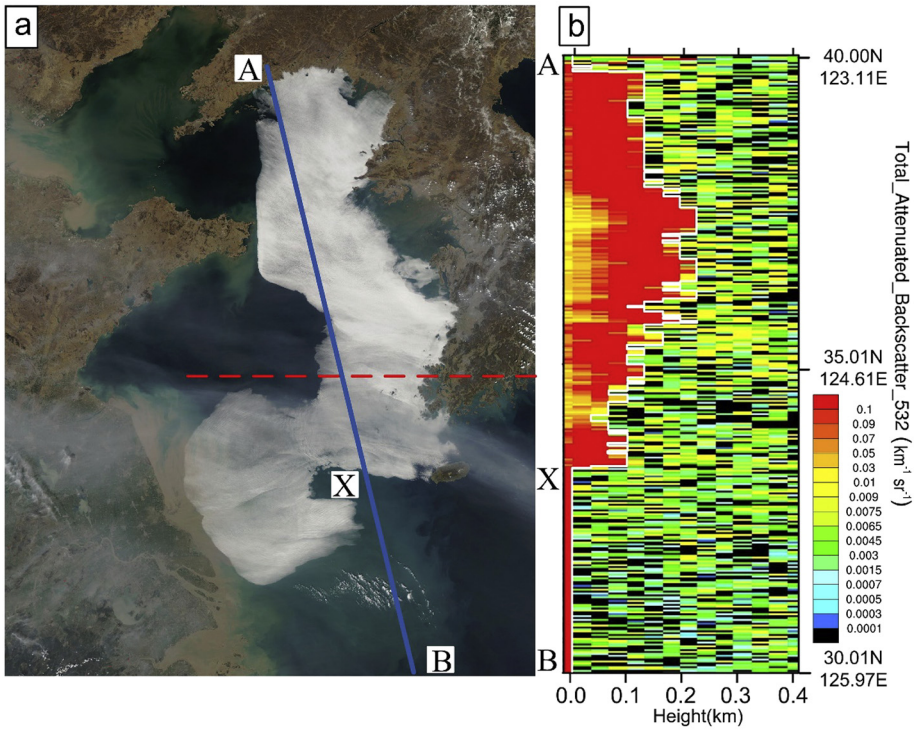

Fig. 2. (a) MODIS visible cloud image at 1300 LST 28 March 2012. The solid blue line AB shows the orbital track of CALIPSO, and the dashed red line is used to differentiate the thick (northern) and shallow (southern) sea fog patches. (b) Representation of fog-top height diagnosed from total 532 nm attenuated backscatter signals of the CALIPSO data along line AB. Total attenuated backscatter signals plotted in yellows and reds ($> 0.0065\,km^{-1}\,sr^{-1}$) indicate sea fog, and the fog-top is shown by the white edges atop the red shading. Label X in both (a) and (b) shows the southern boundary of sea fog patch. (For interpretation of the references to colour in this figure legend, the reader is referred to the web version of this article.)

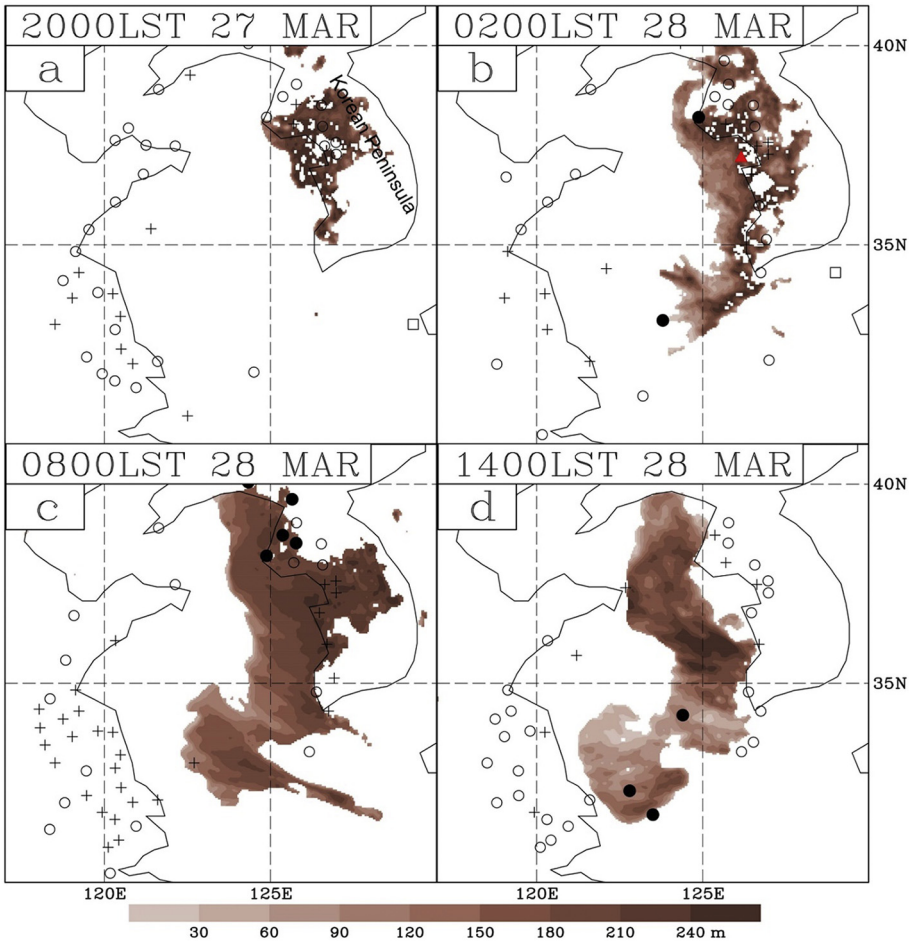

Fig. 3. Evolution of observed sea fog area (shaded; fog-top height is shaded in brown). The location of buoy Deokjeokdo (DK; red triangle) is marked in (b). The symbols ●, + and ○ represent the observed visibility with values 0–1 km, 1–5 km and 5–10 km, respectively. (For interpretation of the references to colour in this figure legend, the reader is referred to the web version of this article.)

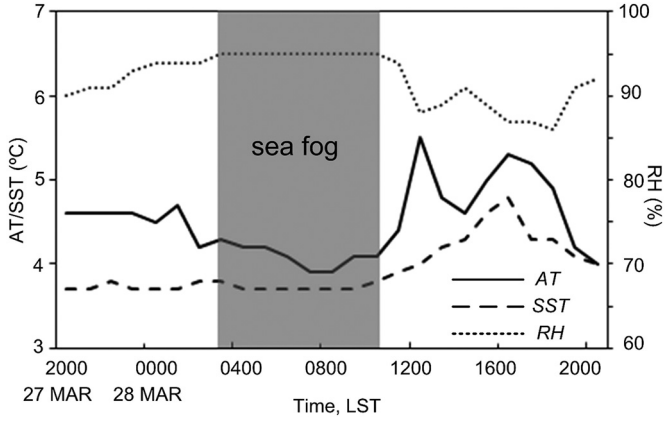

Fig. 4. Time series of air temperature (*AT*, solid line), sea surface temperature (*SST*, dashed line) and relative humidity (*RH*, dotted line) measured at buoy Deokjeokdo (red triangle in Fig. 3b). Grey area denotes the period of sea fog occurrence with $RH \geq 95\%$.

Fig. 4). It is inferred that the derived sea fog above the buoy could be regarded as stratus during this period. As the surface air temperature at the buoy significantly dropped after 0300 LST 28 March, sea fog patch became widespread and maintained over the YS (Fig. 3c). The sea fog became mature by 1400 LST 28 March with thick fog patch distributed over cold water along the western coast of the Korean peninsula and shallow fog patch developed over the southwestern YS with low *SST* (Fig. 3d).

2.2. Model configuration

The WRF model uses two one-way nested domains (D1 and D2 in Fig. 1), which are centered at (35 ° N, 123 ° E) with horizontal resolutions of 30 and 10 km, respectively. The model physics configuration includes the Lin MP scheme (Lin et al., 1983), the Kain-Fritsch cumulus scheme (Kain, 2004; Kain and Fritsch, 1990), the Rapid Radiative Transfer Model for General circulation models (RRTMG) shortwave/longwave radiation (RA) schemes (Iacono et al., 2008), and the Noah LSM (Chen and Dudhia, 2001). The PBL parameterization is set to the YSU-BUOY scheme (Ghonima et al., 2017), which is based on the YSU scheme and proposed to take into account the conserved ice-liquid-water potential temperature within the cloud layer and the turbulent mixing driven by longwave radiative cooling atop the cloud. In order to apply this scheme to advection fog modeling, the cloud base is redefined as the surface. The companion MM5 Monin-Obukhov surface layer scheme (Jiménez et al., 2012; Zhang and Anthes, 1982) is chosen.

The initial and lateral boundary conditions are extracted from the National Centers for Environmental Prediction (NCEP) Global Forecast System (GFS) analysis (0.5 ° × 0.5 °, 3 hourly). The cycling-3DVar data assimilation method (Gao et al., 2010) is performed for both domains with a cycle interval of 3 h from 0800 to 2000 LST 27 March 2012. The assimilated data include sounding, surface measurements, and satellite-derived temperature profiles. The model is integrated for a total of 24 h from 2000 LST 27 March to 2000 LST 28 March 2012. Tests of various spin-up time have been conducted, and the results show that longer spin-up time does not necessarily improve the model performance in terms of reproducing the fog event. Model outputs at 10-min interval are used for detailed analysis of physical processes associated with the sea fog event.

2.3. Experimental design

The WRF model uses a terrain-following hydrostatic-pressure vertical coordinate with η levels defined as $\eta = (p - p_t)/(p_s - p_t)$ ranging from 1.0 to 0.0, where p is pressure, and the subscripts "t" and "s" denote model top and surface, respectively. In the WRF model, vertical velocity, vertical turbulent fluxes and eddy diffusivities are computed at the full-η levels (η_n), while horizontal wind components and thermodynamic prognostic variables are assigned to the half-η levels (z_n), which are located at the middle of two adjacent full-η levels (Shin et al., 2012; Skamarock et al., 2008). The lowest model level height z_1 is determined by the value of η_2 (note $\eta_1 = 1.0$) when p_t is chosen.

The baseline experiment uses 42 full-η levels[2] with p_t at 50 hPa. The corresponding z_1 is 28 m. To examine the importance of the lowest model level in resolving sea fog processes, one lower full-η level is added as η_2. Additional 6 sensitivity experiments with lower z_1 (i.e., 22, 14, 8, 4, 1, and 0.4 m) and almost the same layer thickness between z_1 and z_2 are conducted (Table 2). These experiments are named as Exp-L28, Exp-L22, Exp-L14, Exp-L8, Exp-L4, Exp-L1, and Exp-L0.4, respectively.

2.4. Observations and sea fog diagnostics used for evaluation

Model simulations are evaluated over both the ocean and land for a comprehensive assessment of the performance of experiments with different z_1. Since routine in-situ measurements are sparse over sea, surface observations over land are more convinced. The continental datasets include: 2-m temperature (*T2*) collected from the Integrated Surface Database (ISD) of NOAA's National Centres for Environmental Information (NCEI) (see the site locations in Fig. 5), the selected sounding data at Zhangqiu, China (denoted by black dot and ZQ in Fig. 1) that have more levels of observation in the lower troposphere compared to routine sounding data, and sounding data collected at Osan, Korea (black dot and OS in Fig. 1) that contain additional observations at 1400 LST in addition to routine soundings at 0800 and 2000 LST.

Over sea, the numerical experiments are evaluated in terms of simulated sea fog area and fog onset time in D2 using observed sea fog area derived from the MTSAT data (Fig. 3). The region with *LWC* at the lowest model level [hereafter $LWC(z_1)$] $\geq 0.016\ g\ kg^{-1}$ but the fog-top height ≤ 400 m is defined as the simulated sea fog area (Wang et al., 2014; Yang and Gao, 2016; Zhou and Du, 2010). The fog-top height is calculated using the threshold of $LWC \geq 0.016\ g\ kg^{-1}$.

Statistical scores for evaluation of sea fog area are used, including the probability of detection (POD), false alarm ratio (FAR), bias (defined as the ratio of forecast points to observed points with the best value of 1.0), and equitable threat score (ETS) (e.g., Doswell III and Flueck, 1989; Wang et al., 2014; Zhou and Du, 2010).

3. Results

3.1. Sensitivity over land

While our overarching goal is to examine the sensitivity of simulated sea fog to z_1, it is noticed that a too low z_1 may lead to an unreasonable PBL simulation over land (Shin et al., 2012). The z_1 configurations that may lead to such kinds of unreasonable simulations need to be avoided for accurate sea fog simulations since continental PBL along the coastal region affects sea fog formation and evolution near the coast. Thus, we first discuss the reasons for unreasonable continental PBL simulations before we reveal the sensitivity of simulated sea fog to z_1.

[2] η = 1.000, 0.9930, 0.9830, 0.9700, 0.9540, 0.9340, 0.9090, 0.8800, 0.8506, 0.8212, 0.7918, 0.7625, 0.7084, 0.6573, 0.6090, 0.5634, 0.5204, 0.4798, 0.4415, 0.4055, 0.3716, 0.3397, 0.3097, 0.2815, 0.2551, 0.2303, 0.2071, 0.1854, 0.1651, 0.1461, 0.1284, 0.1118, 0.0965, 0.0822, 0.0689, 0.0566, 0.0452, 0.0346, 0.0249, 0.0159, 0.0076, 0.0000, with 10 full-η levels below 850 hPa, the corresponding heights are about 0, 56, 136, 244, 376, 546, 760, 1018, 1284, 1556 m, respectively.

Table 2
Configuration of z_1 in the WRF model.

Experiment	Exp-L28	Exp-L22	Exp-L14	Exp-L8	Exp-L4	Exp-L1	Exp-L0.4
z_1 (m)	28	22	14	8	4	1	0.4
z_2 (m)	96	49	41	36	32	29	28
η_1	1.0	1.0	1.0	1.0	1.0	1.0	1.0
η_2	0.993	0.9945	0.9965	0.998	0.999	0.9997	0.9999
η_3	0.983	0.993	0.993	0.993	0.993	0.993	0.993

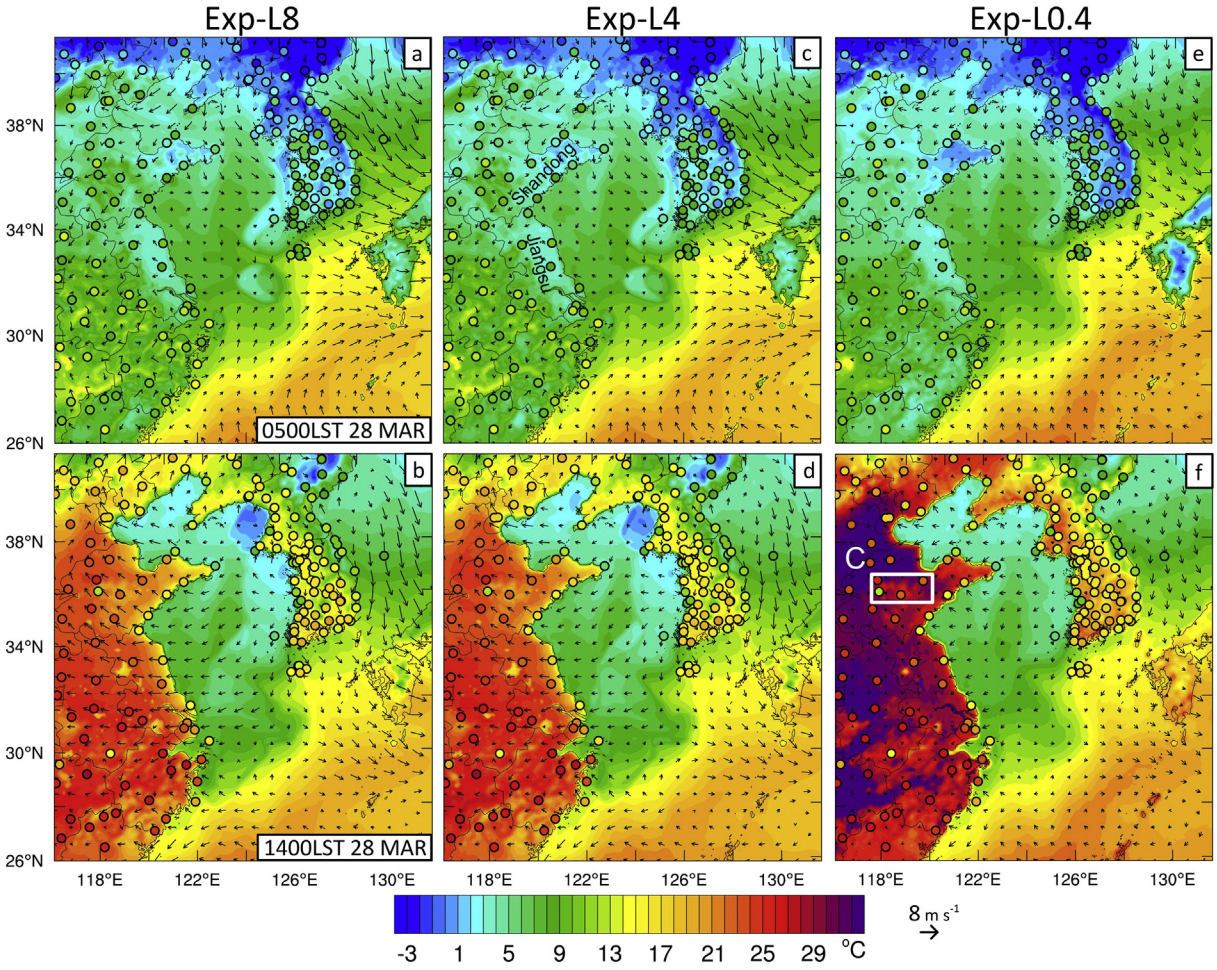

Fig. 5. Spatial distributions of 2-m temperature (*T2*; colour shaded) and 10-m wind fields (vectors) at 0500 LST (a, c, e) and 1400 LST (b, d, f) 28 March 2012 in D2 simulated by (a, b) Exp-L8, (c, d) Exp-L4, and (e, f) Exp-L0.4. Observations of the ISD data are overlaid using shaded circles. (For interpretation of the references to colour in this figure legend, the reader is referred to the web version of this article.)

3.1.1. Temperature at 2 m

To verify the rationality of z_1 in 7 numerical experiments, simulated *T2* over land is evaluated using surface observations from the ISD. As summarized in Table 3, simulations with z_1 varying between 28 and 8 m underestimate *T2* by ~3.7 °C in average at 0500 LST March 28 and overestimate *T2* by ~0.5 °C at 1400 LST. Fig. 5a, b illustrate that *T2* simulated by Exp-L8 agree relatively well with the observations, with a correlation coefficient of 0.701/0.544 at 0500/1400 LST. However, deviations of *T2* simulated by Exp-L4 are larger, with a mean bias (MB) of −3.9/1.1 °C and a normalized mean bias (NMB) of −38.9%/6.4% at 0500/1400 LST (Table 3). The model performance is obviously poor along the coastal region of Shandong and Jiangsu (see their locations in Fig. 1) in China (Fig. 5c, d). When z_1 is further reduced to below 4 m, the performance gets even worse. Exp-L0.4 has MB up to −4.7/6.9 °C, RMSE larger than 6.1/10.5 °C, and NMB of −46.2%/40.7% at 0500/1400 LST (Table 3).

The ZQ station is located at Shandong province, where the sensitivity of *T2* to z_1 is distinct. In-situ surface observations at ZQ are selected to evaluate temporal evolution of *T2* (Fig. 6a). Experiments with z_1 varying between 28 and 8 m show relatively good agreements with the observations and the results are almost insensitive to z_1, especially in the daytime. Nevertheless, results of experiments with z_1 below 8 m deviate from the measurements and become colder/warmer during the night time/daytime with a reducing z_1, for example, *T2* at 1400 LST 28 March is overestimated by ~7 °C in Exp-L0.4 (Fig. 6a).

3.1.2. PBL height

Sounding observations from OS and ZQ are used to examine simulated PBL structure. In terms of OS at 1400 LST 28 March, the diagnostic convective PBL height h using the 1.5-theta-increase method (Nielsen-Gammon et al., 2008; Hu et al., 2010) is ~1.2 km, which is comparable to the simulated h as z_1 ranges from 28 to 8 m (Fig. 6b).

Table 3
Statistics[a] of 2-m temperature at 0500 and 1400 LST 28 March from observations at most stations[b] over mainland China and the Korean peninsula and from simulations in seven experiments.

	0500 LST 28 MAR							1400 LST 28 MAR						
	Exp-L28	Exp-L22	Exp-L14	Exp-L8	Exp-L4	Exp-L1	Exp-L0.4	Exp-L28	Exp-L22	Exp-L14	Exp-L8	Exp-L4	Exp-L1	Exp-L0.4
Mean observation	10.114	10.114	10.114	10.114	10.114	10.114	10.114	16.889	16.889	16.889	16.889	16.889	16.889	16.889
Mean simulation	6.592	6.472	6.279	6.215	6.183	5.964	5.442	17.312	17.301	17.330	17.434	17.973	20.351	23.770
Number of data	375	375	375	375	375	375	375	488	488	488	488	488	488	488
Corr	0.704	0.704	0.703	0.701	0.706	0.716	0.718	0.552	0.549	0.549	0.544	0.535	0.478	0.350
MB	−3.522	−3.643	−3.835	−3.899	−3.931	−4.150	−4.672	0.423	0.412	0.442	0.545	1.085	3.462	6.881
RMSE	5.345	5.419	5.555	5.609	5.612	5.733	6.117	6.362	6.396	6.385	6.442	6.582	7.726	10.560
NMB	−0.348	−0.360	−0.379	−0.385	−0.389	−0.410	−0.462	0.025	0.024	0.026	0.032	0.064	0.205	0.407

[a] The statistical metrics include: correlation coefficient (corr), mean bias (MB), root mean-square error (RMSE), normalized mean bias (NMB).
[b] Data from total 1188 stations are available for studied case.

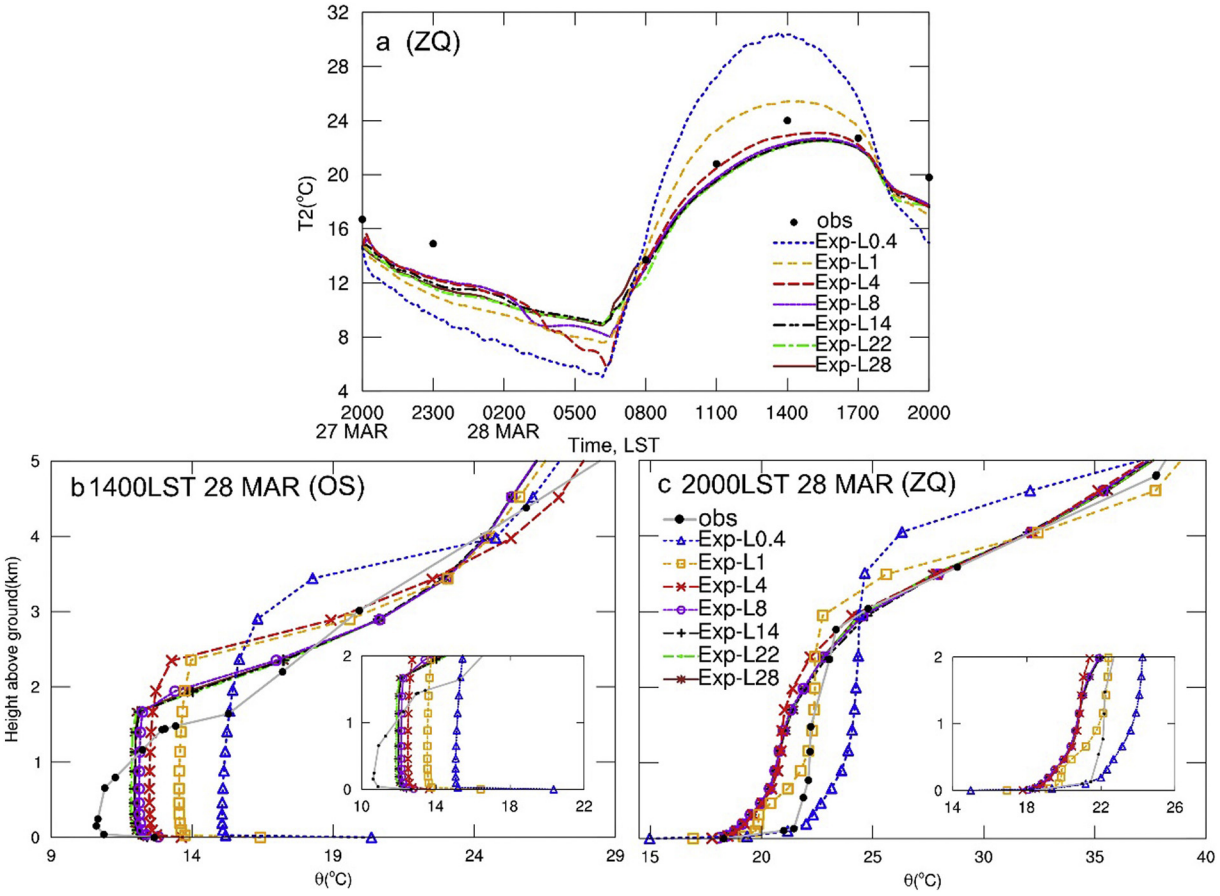

Fig. 6. (a) Time series of 2-m temperature (*T2*) from Exp-L28, Exp-L22, Exp-L14, Exp-L8, Exp-L4, Exp-L1, and Exp-L0.4 overlaid with in-situ surface observations (black dots) at Zhangqiu from 2000 LST 27 March to 2000 LST 28 March 2012. Profiles of potential temperature (θ) from Exp-L28, Exp-L22, Exp-L14, Exp-L8, Exp-L4, Exp-L1, and Exp-L0.4 overlaid with sounding observations (grey line with black dots) at (b) Osan at 1400 LST and (c) Zhangqiu at 2000 LST 28 March 2012. In both (b) and (c), the vertical axis refers to the height above ground level (AGL) and each inset provides a closer look at θ profiles within 1.5 km AGL.

Note that the 1.5-theta-increase method defines the convective h as the level where the potential temperature first exceeds the minimum potential temperature within the PBL by 1.5 K. However, h is overestimated by ~1.1 km when z_1 reduces to 4 m. Excessively large h (> 2.5 km) is simulated with the lower z_1 (Exp-L1 and Exp-L0.4). For ZQ at 2000 LST, experiments with z_1 varying between 28 and 8 m yield similar stable PBL structures, while the results from experiments with z_1 below 8 m are greatly different to each other (Fig. 6c).

Therefore, these 7 sensitivity experiments can be classified into 2 groups according to the above evaluations, i.e., Group-A (Exp-L28, Exp-L22, Exp-L14, and Exp-L8) and Group-B (Exp-L4, Exp-L1 and Exp-L0.4). Simulated surface temperature and h over land in Group-A are comparable to the observations with less sensitivity to z_1, while the results in Group-B deviate from the measurements and are significantly sensitive to z_1. Daytime average h over land within frame C (shown in Fig. 5f) simulated by experiments of Group-B is enormously high. The maximum value up to 5 km in Exp-L0.4 is considerably irrational (Fig. 7a).

Both Shin et al. (2012) and Lemone et al. (2013) found that h over land is highly sensitive to z_1 in the YSU scheme. In this scheme, h is defined as the lowest altitude where the bulk Richardson number (Ri_b) between the surface and this altitude approaches the critical Richardson number, which is set to 0.0/0.25 in unstable/stable regimes over land (Noh et al., 2003; Hong, 2010). In the determination of Ri_b under

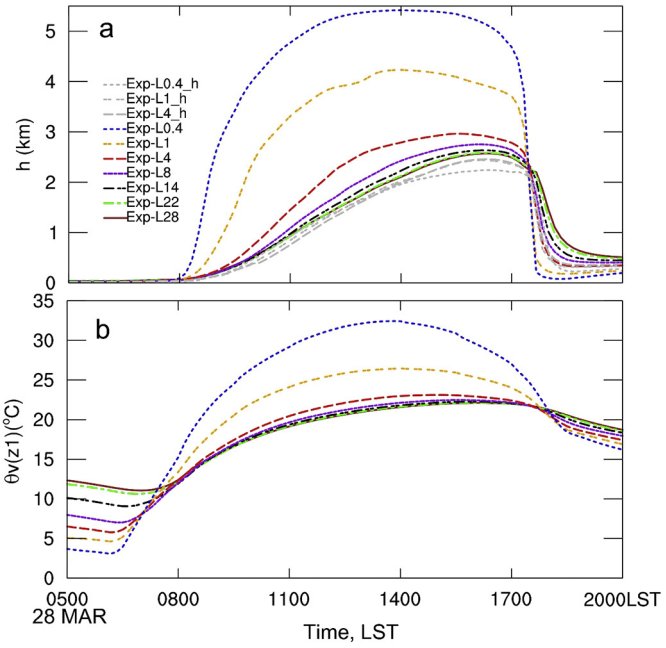

Fig. 7. Time series of (a) PBL height (h) and (b) virtual potential temperature (θ_v) at z_1 averaged over the land region marked by C in Fig. 5f from Exp-L28, Exp-L22, Exp-L14, Exp-L8, Exp-L4, Exp-L1, and Exp-L0.4. The grey lines represent h from Exp-L4_h, Exp-L1_h, and Exp-L0.4_h, in which the diagnostic of h has been modified in the YSU scheme. (For interpretation of the references to colour in this figure legend, the reader is referred to the web version of this article.)

convective regimes, the appropriate near-surface temperature (θ_s) is calculated based on virtual potential temperature (θ_v) at z_1 and the temperature excess of thermals by:

$$\theta_s = \theta_v(z_1) + \theta_T \tag{1}$$

In the convective PBL, the near surface air is super-adiabatic and θ_v increases more quickly than adiabatic lapse rate of 9.8 °C km^{-1} when the altitude approaches the surface. The calculation of θ_s by Eq. (1) is highly dependent on $\theta_v(z_1)$ (Fig. 7b), and θ_s gets too large (which leads to too high h) as z_1 is too low (e.g., 4 m in Shin et al., 2012 and 5 m in Lemone et al., 2013). To improve the calculation of h under unstable conditions when z_1 is low, Shin et al. (2012) applied a scaling factor to θ_T when z_1 is within the surface layer:

$$\theta_s = \theta_v(z_1) + \theta_T \cdot min\left(\frac{z_1}{0.1h}, 1\right) \tag{2}$$

In the present study, Eq. (2) appears to work for PBL calculation when z_1 is higher than 4 m, but h is still be overestimated when z_1 is lower than 4 m (Fig. 7a). Furthermore, the temperature difference between z_1 and z_2 increases more significantly than that of Group-A (0.3–0.7 °C) with a value up to 4.8 °C as z_1 is further reduced to below 4 m, which indicates that a too low z_1 may constrain the interaction between the surface layer and PBL, leading to overestimated θ_s and h. Due to $\theta_v(z_2)$ seems to be less sensitive to z_1 than $\theta_v(z_1)$, an additional experiment of replacing $\theta_v(z_1)$ with $\theta_v(z_2)$ in Eq. (2) is conducted when z_1 is lower than 4 m, which promotes a better estimation of h (grey lines in Fig. 7a). The results suggest that a more appropriate calculation of θ_s is needed if the WRF model with the YSU scheme is used with z_1 lower than 4 m.

3.2. Sensitivity over sea

As shown in experiments with low z_1 in Group-B, the model has deficiencies in modeling continental PBL, thus they (with $z_1 \leq$ 4 m) are not recommended for the PBL simulation over sea. For this reason, only results from Group-A with z_1 varying from 28 to 8 m are evaluated in terms of the model capability to reproduce the sea fog event.

3.2.1. Sea fog area

Compared to the observed sea fog area (Fig. 8a–e), 4 experiments in Group-A can not only reproduce the shape of sea fog area, but also capture its temporal evolution to varying degrees (Fig. 8f–y). The sea fog forms earlier and fog area increases progressively when z_1 decreases from 28 to 8 m (e.g., Fig. 8h, m, r, w). The statistical scores for these simulated sea fog areas are listed in Table 4. ETS is a comprehensive verification score that considers combined effects (POD, FAR, and missing rate, etc.) (Zhou et al., 2011). Although both POD and FAR simultaneously increase with a lowering z_1, ETS still increases, for the improvement of POD overwhelms the deterioration of FAR. The increase in ETS indicates that the horizontal distribution of simulated sea fog gets gradually improved and becomes more consistent with the observation. Exp-L8 performs best with POD (0.499) twice as large as that of Exp-L28, and its ETS (0.269) is larger than that of Exp-L28 by 0.1. The bias of 1.014 in Exp-L8 means that the size of simulated sea fog area is comparable to the observed area. As z_1 reduces, the shallow sea fog patch (frame D in Fig. 8x) characterized by an advection fog extends remarkably, implying a greater sensitivity to z_1 than the thick one to the north (e.g., Fig. 8j, o, t, y).

3.2.2. Timing of sea fog onset and fog density

For the shallow sea fog patch in experiments of Group-A, timing of sea fog onset and fog density denoted by average $LWC(z_1)$ vary greatly (Fig. 9a). The formation of sea fog in Exp-L8 is the earliest at 2150 LST 27 March, which is consistent with the observation (between 2100 and 2200 LST 27 March). The sea fog in Exp-L14 lags ~1 h 30 min in comparison to that in Exp-L8, while the onset time in both Exp-L22 and Exp-L28 are later than 0000 LST 28 March. A lower z_1 leads to not only an earlier formation of sea fog, but also a larger fog density before 0800 LST 28 March. As shown in Fig. 9a, the maximum of $LWC(z_1)$ gradually increases from 0.7 to 1.0 g kg^{-1} when z_1 varies from 28 to 8 m at the early stage of sea fog formation. It should be noted that the $LWC(z_1)$ begins to increase when the lowering of $\theta_v(z_1)$ happens (Fig. 9b), and the maximum $LWC(z_1)$ matches well with the minimum $\theta_v(z_1)$ for each experiment. Therefore, the variation of $LWC(z_1)$ appears to be highly correlated with the corresponding $\theta_v(z_1)$, which is also stated by Oliver et al. (1978).

3.3. Explanation for the impacts of z_1 on simulating sea fog process

The evaluation of results in Group-A shows that $LWC(z_1)$ is influenced by $\theta_v(z_1)$, thus the response of simulated sea fog to z_1 can be attributed to the sensitivity of $\theta_v(z_1)$ to z_1. Such a sensitivity of simulated sea fog to z_1 is also found in Group-B. The sea fog forms earlier, but the fog height and its area are severely underestimated as z_1 reduces (e.g., Fig. 8 ab, ag, al). Note that the initial fog patches to the south in Exp-L1 and Exp-L0.4 tend to dissipate quickly (Fig. 8 af, ak), while it can redevelop in Exp-L1. In addition, the obvious change of thick fog patch may be associated with the unreasonable PBL simulation over land as z_1 below 4 m. Our principle concern is the sensitivity of advection fog simulation to z_1. Therefore, understanding of how z_1 affects $\theta_v(z_1)$ and how $\theta_v(z_1)$ consequently alters advection fog processes can help explain the impacts of z_1 on simulation of sea fog process.

When warm air mass passes over colder sea surface during an advection fog event, the air-sea interaction leads to the lowering of $\theta_v(z_1)$ through downward (negative) sensible heat flux (HFX) in the surface layer, which is the major thermal forcing for the sea fog onset compared to other surface fluxes. These surface fluxes can be parameterized by using the lower boundary conditions, i.e., SST, winds and roughness length. Such conditions differ slightly in simulations with various z_1 (not shown). Only sufficient decrease in $\theta_v(z_1)$ can result in fog

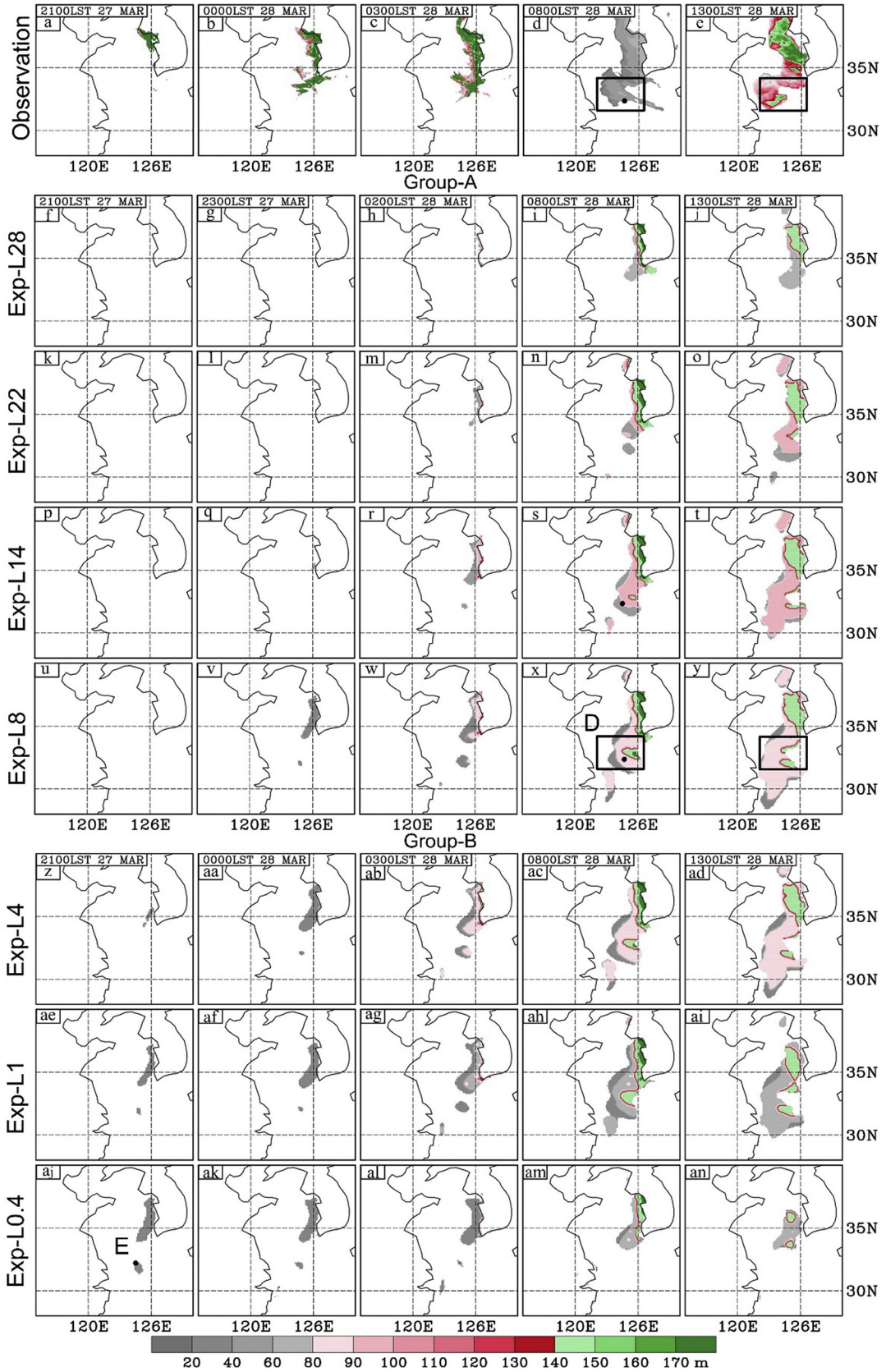

Fig. 8. Spatial distributions of (a-e) observed and simulated sea fog from (f-j) Exp-L28, (k-o) Exp-L22, (p-t) Exp-L14, (u-y) Exp-L8, (z; aa-ad) Exp-L4, (ae-ai) Exp-L1, and (aj-an) Exp-L0.4 (colour shaded represents fog-top height). (For interpretation of the references to colour in this figure legend, the reader is referred to the web version of this article.)

Table 4
Statistical scores of the experiments in Group-A for simulated sea fog area.

Experiment	POD	FAR	bias	ETS
Exp-L28	0.258	0.462	0.480	0.170
Exp-L22	0.325	0.470	0.613	0.199
Exp-L14	0.435	0.467	0.817	0.243
Exp-L8	0.499	0.508	1.014	0.269

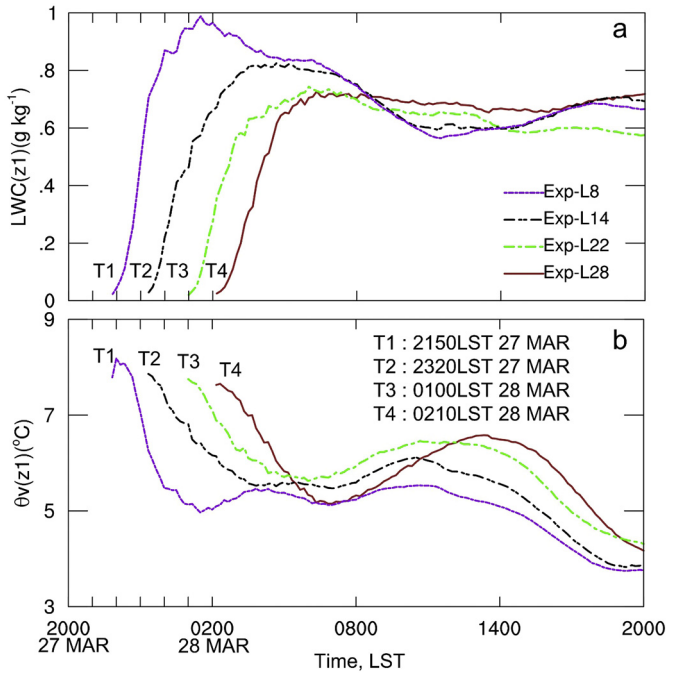

Fig. 9. Temporal evolutions of (a) *LWC* at $z_1 \geq 0.016\,\mathrm{g\,kg^{-1}}$ and (b) virtual potential temperature (θ_v) at z_1 averaged over the shallow sea fog patch marked by D in Fig. 8x from Exp-L28, Exp-L22, Exp-L14, and Exp-L8. The sea fog onset time in these experiments are labelled by T1 to T4, respectively.

formation near the sea surface. Based on the value of $\theta_v(z_1)$, the YSU PBL scheme first estimates h, upon which the vertical mixing is determined. The vertical extension of such an initial surface fog primarily depends on the turbulent mixing between z_1 and its upper level. According to a budget analysis, total $\theta_v(z_1)$ tendency (F_{θ_v}) can be written as:

$$F_{\theta_v} = F_{\theta_v,\mathrm{PBL}} + F_{\theta_v,\mathrm{RA}} + F_{\theta_v,\mathrm{MP}} \tag{3}$$

where F_{θ_v}, PBL, F_{θ_v}, RA and F_{θ_v}, MP represent the tendencies of $\theta_v(z_1)$ due to schemes of PBL, RA and MP, respectively. F_{θ_v}, PBL primarily covers surface sensible heat exchange (Eq. (4); Stensrud, 2007) and eddy diffusivity from η_2 (Eq. (5); Hu and Xue, 2016; Stensrud, 2007). They are expressed as follows:

$$F_{\theta_v,HFX} = \frac{HFX}{\rho c_p \times (2z_1)} \tag{4}$$

$$F_{\theta_v,\mathrm{Diffusion}} = K_h(\eta_2) \times \frac{\theta_v(z_2) - \theta_v(z_1)}{(2z_1) \times (z_2 - z_1)} \tag{5}$$

In addition, F_{θ_v}, RALW represents the $\theta_v(z_1)$ tendency due to longwave radiation (Eq. C11 in Dudhia, 1989), which plays a more dominant role for $\theta_v(z_1)$ than shortwave radiation in the RA scheme. Both F_{θ_v}, RALW and F_{θ_v}, MP are associated with the condensation of $LWC(z_1)$ in sea fog simulation, but they have opposite effects on $\theta_v(z_1)$, i.e., the former has a cooling effect, whereas the latter has a heating effect. In contrast, F_{θ_v}, RALW makes a primary contribution to the decrease in $\theta_v(z_1)$ after fog formation.

In order to identify the influences of various z_1 on the above physical processes in terms of different stages of sea fog event, Exp-L8 and Exp-L14 from Group-A and Exp-L0.4 from Group-B are deliberately selected for detailed study. Note that Exp-L8 is the one with the best performance, which will be explored as a baseline. Fig. 10 shows the temporal evolution of θ_v and the mixing ratio of water vapor (qv) as well as heat diffusivity coefficient (K_h) at point E (shown in Fig. 8 aj and also marked in Fig. 8d, s, x) below ~300 m from 2000 LST 27 March to 1400 LST 28 March. Time series of $\theta_v(z_1)$, $\theta_v(z_2)$, *HFX*, F_{θ_v} and tendencies of $\theta_v(z_1)$ due to primary physical processes from 2000 LST 27 March to 0600 LST 28 March at point E are illustrated in Fig. 11. Both upward cooling from the sea surface before sea fog onset and longwave radiative cooling of fog droplets after that can be easily recognized from the time series of F_{θ_v} (Fig. 11c), which is the time rate of $\theta_v(z_1)$, especially for Exp-L14 and Exp-L8. As is clear from Fig. 11d and e, two primary tendencies of $\theta_v(z_1)$ within the PBL (F_{θ_v}, *HFX* and F_{θ_v}, Diffusion) become systematically fast when z_1 approaches the surface. This is attributed to the heat capacity of the air in the lowest model layer, which progressively reduces as z_1 becomes lower, leading to a quick response of $\theta_v(z_1)$. The tendency of $\theta_v(z_1)$ due to RALW mainly relies on the fog density (Fig. 11f).

3.3.1. Sea fog formation at z_1

Upward cooling from the cold sea surface is essential for the occurrence of advection fog. In Exp-L8, the cooling rate of $\theta_v(z_1)$ caused by negative *HFX* (upward cooling; Fig. 11b) is up to 0.24 °C per 10 min (Fig. 11d), and $\theta_v(z_1)$ decreases by 3.5 °C in 3.5 h due to its continuous cooling (Fig. 11a). Meanwhile, qv at z_1 is 7.0–7.5 $\mathrm{g\,kg^{-1}}$ (Fig. 10e), which supplies a sufficient water vapor condition for sea fog formation under enough cooling. In response to the cooling and moistening of the air at z_1 described above, sea fog forms at 2330 LST 27 March (see S2 in Fig. 10b). The cooling rate caused by *HFX* in Exp-L0.4 is 2.7 °C per 10 min, which is larger than that in Exp-L8, while the maximum cooling rate in Exp-L14 is only 0.12 °C per 10 min (Fig. 11d). Since z_1 dominates the tendency of $\theta_v(z_1)$ due to *HFX* (Eq. (4)), $\theta_v(z_1)$ responds quickly (slowly) to the upward cooling if z_1 is low (high) with small (large) heat capacity in the lowest model layer. More rapid decrease in $\theta_v(z_1)$ in Exp-L0.4 leads to an earlier fog formation at 2010 LST 27 March (see S3 in Fig. 10c). The sea fog onset time in Exp-L14 (see S1 in Fig. 10a) lags 3 h 30 min than that in Exp-L8. A later fog onset leads to a smaller fog area at the same time (Fig. 8r, w).

3.3.2. Upward extension of sea fog from z_1 to z_2

After the sea fog forms initially at z_1 in Exp-L8, sea fog extends upward quickly from z_1 to z_2 (Fig. 10b). Once the fog occurs, the longwave radiative cooling of fog droplets starts to take effect and gradually becomes dominant (Fig. 11f), which makes $\theta_v(z_1)$ to be as low as ~3 °C till 0600 LST 28 March. Low temperature corresponds to low saturation vapor pressure, which is favorable for the increase of relative humidity and the maintenance of sea fog (Fig. 10b). In the meantime, θ_v at z_2 [hereafter $\theta_v(z_2)$] progressively reduces (Fig. 11a) due to turbulent mixing between z_1 and z_2. The turbulent mixing transports warmer air from z_2 to z_1 (Fig. 11e) and brings colder air from z_1 to z_2. When the difference between $\theta_v(z_2)$ and $\theta_v(z_1)$ increases to ~3 °C (Fig. 11a), $\theta_v(z_2)$ is cold enough to allow sea fog formation at z_2, which leads to upward extension of fog soon after sea fog formation at z_1 (Fig. 10b).

In Exp-L8, the cooling effect due to negative *HFX* diminishes when $\theta_v(z_1)$ gradually decreases to *SST* (Fig. 11d). The cooling effect from longwave radiation of fog droplets overwhelms the heating effect of turbulent mixing (Fig. 11e, f). The $\theta_v(z_1)$ continues reducing and it turns into lower than *SST* approximately after 0000 LST 28 March (Fig. 11a, d). Although both the positive *HFX* below z_1 and the turbulent mixing above z_1 can bring warm air mass to z_1, the cooling effect from longwave radiation of fog droplets still dominates, leading to a large decrease in $\theta_v(z_1)$ (Fig. 11a). Such decrease in Exp-L8 is conducive to the maintaining of sea fog at z_1 and its upward extension towards z_2.

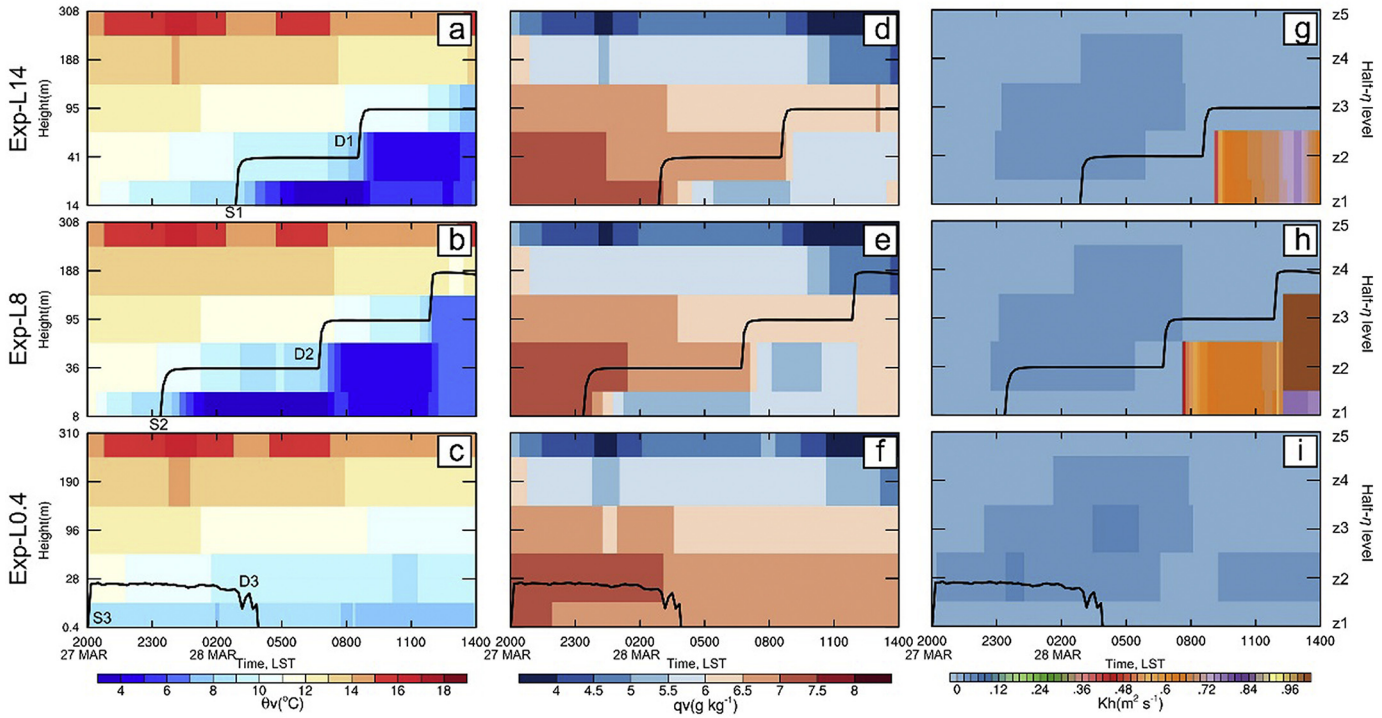

Fig. 10. Time-height diagrams of (a-c) virtual potential temperature (θ_v), (d-f) mixing ratio of water vapor (qv) and (g-i) heat diffusivity coefficient (K_h) at point E shown in Fig. 8 aj simulated by (a, d, g) Exp-L14, (b, e, h) Exp-L8 and (c, f, i) Exp-L0.4. Black lines denote LWC with value of 0.016 g kg^{-1} outlining sea fog top. The sea fog onset time in these experiments are labelled by S1 to S3, respectively. D1 to D3 denote the sea fog development or dissipate time in these experiments. (For interpretation of the references to colour in this figure legend, the reader is referred to the web version of this article.)

However, $\theta_v(z_1)$ in Exp-L0.4 responds more quickly to heating from turbulent mixing than it does in Exp-L8 because of the lower z_1 (Eq. (5)), which is similar as the response to *HFX*. The maximum turbulent heating rate that is up to 2.8 °C per 10 min is over 15 times larger than that in Exp-L8 (Fig. 11e). After 2010 LST 27 March, this strong turbulent heating offsets the longwave radiative cooling of fog droplets soon (Fig. 11e, f). The air mass at the lowest model level in Exp-L0.4 is unable to be cooled sufficiently. The cooling magnitude after sea fog onset is slight, which is far less than that of Exp-L8 by ~5 °C (Fig. 11a). Since $\theta_v(z_1)$ is not cold enough, the sea fog is unable to extend towards z_2 after 0300 LST 28 March (see D3 in Fig. 10c). Subsequently, the warmer condition with higher temperature of ~8 °C allows less fog droplets, and strong turbulent mixing of 0.06 m^2 s^{-1} leads to rapid dispersal of sea fog before 0400 LST 28 March (Fig. 10c, f, i). As a result, the shallow fog area is underestimated in Exp-L0.4 (e.g., Fig. 8 al).

The phase of upward fog extension to z_2 in Exp-L14 resembles that in Exp-L8, and the longwave radiative cooling of fog droplets also plays a dominant role. However, the higher z_1 in Exp-L14 leads to a weaker cooling from longwave radiation (Fig. 11f), because less $LWC(z_1)$ is produced due to warmer air mass.

The above analysis indicates that both the cooling effect from longwave radiation of fog droplets and the heating effect of turbulent mixing after sea fog onset are significantly influenced by the value of z_1, and the balance between them is crucial for the upward extension of sea fog to z_2.

3.3.3. Further vertical development of sea fog

The sea fog in Exp-L8 further develops vertically after 0600 LST 28 March (see D2 in Fig. 10b), when warm air with qv of ~6.5 g kg^{-1} is entrained into the fog top (Fig. 10e). The entrained water vapor condenses into liquid water due to low $\theta_v(z_2)$ of ~8 °C, and then fog droplets can be further cooled via longwave radiation effect (Fig. 10b). With the accumulation of LWC near the fog top, the fog layer deepens due to the turbulent mixing of 0.06 m^2 s^{-1} (Fig. 10h). A similar development process can also be seen in Exp-L14, but it is delayed by ~2 h (see D1 in Fig. 10a) due to the slower decrease in $\theta_v(z_2)$. After 1100 LST 28 March, the fog layer in Exp-L8 continues deepening due to the appropriate thermal (lower temperature) and dynamic (turbulent mixing and entrainment) conditions as described above.

During the further development stage, the maximum LWC tends to increasingly change from the bottom towards the fog top (Fig. 12a, b) (Bergot et al., 2007; Tardif, 2007), which is caused by the cold maximum near the fog top (shown in Fig. 10a, b). The maximum cooling rate of θ_v due to longwave radiation (Fig. 12c, d) determines the location of temperature minimum (Findlater et al., 1989; Koračin et al., 2001; Lamb, 1943; Oliver et al., 1978). Fog droplets aloft are heavy enough to mix downward under unstable conditions (Douglas, 1930; Lamb, 1943), resulting in intensive turbulent mixing (shown in Fig. 10g, h). This turbulent mixing is favorable for the maintenance of a well-developed sea fog layer (Findlater et al., 1989; Koračin et al., 2005a, 2014; Oliver et al., 1978).

4. Conclusions and discussion

Previous studies have stated the critical role of the lowest model layer in vertically resolving the near-surface and PBL processes in numerical simulations. Most of these studies focused on the impacts of the lowest model level height (z_1) on simulating phenomena/processes in continental PBL. However, understanding of its roles in simulating marine atmospheric boundary layer processes (e.g., sea fog) is still limited. The present study examines impacts of z_1 on simulating an advection fog formed over the Yellow Sea on 27 March 2012 using the WRF model. Seven experiments using the YSU-BUOY PBL scheme are conducted with different values of z_1 (28, 22, 14, 8, 4, 1 and 0.4 m).

Over land, surface temperature and PBL height are reasonably reproduced when z_1 varies between 28 and 8 m, and the model results are insensitive to z_1. However, with z_1 below 8 m, daytime surface temperature is overestimated and the convective PBL becomes irrationally

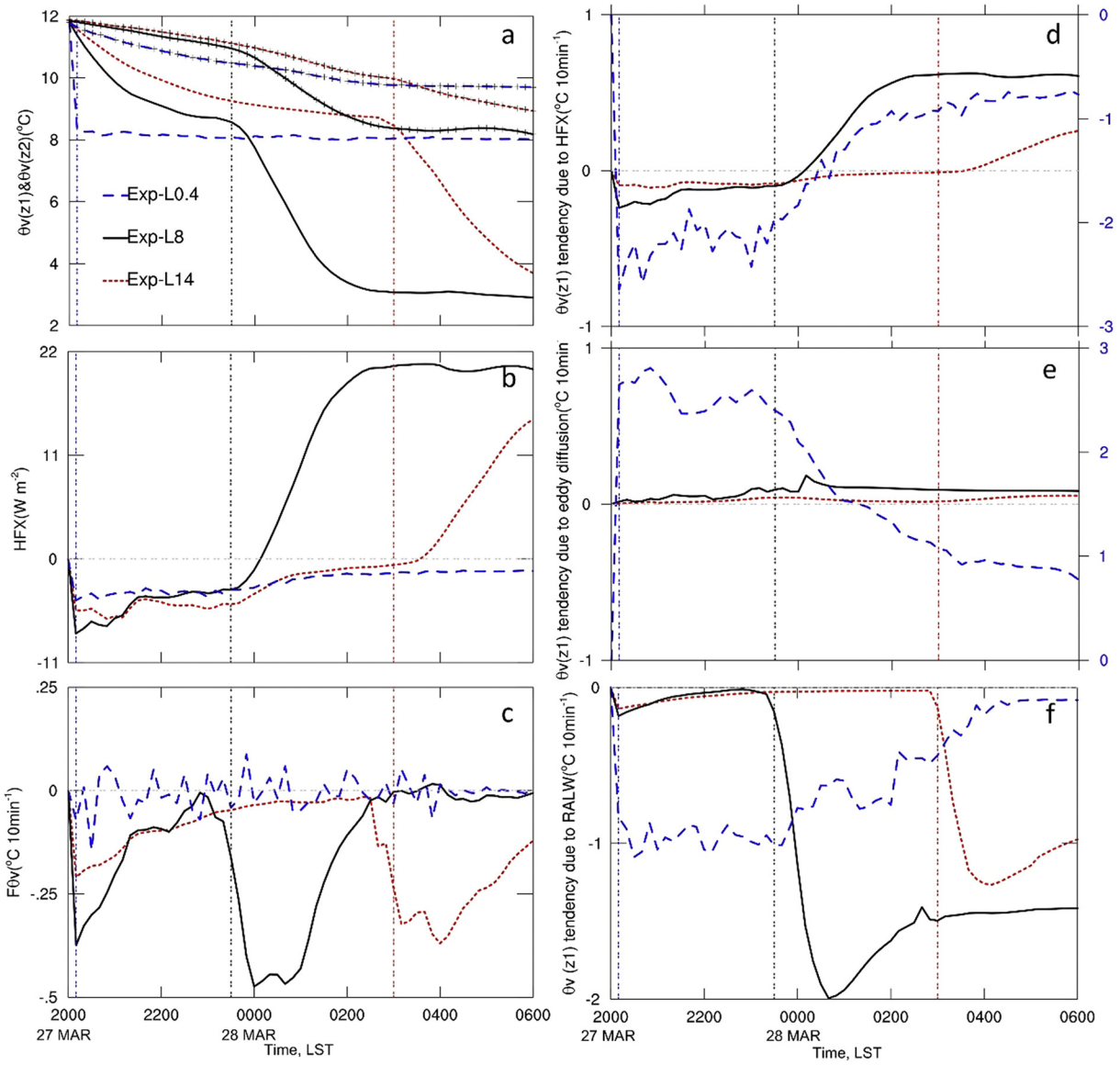

Fig. 11. Temporal evolutions of (a) virtual potential temperature (θ_v) at z_1 and z_2 (lines with "+" markers), (b) surface sensible heat flux (*HFX*), (c) total $\theta_v(z_1)$ tendency (F_{θ_v}), and $\theta_v(z_1)$ tendency due to (d) sensible heat exchange of *HFX*, (e) eddy diffusion above z_1, and (f) RALW processes for formation, extension and maintenance phases of sea fog from 2000 LST 27 March to 0600 LST 28 March 2012 in Exp-L14 (dotted red line), Exp-L8 (solid black line) and Exp-L0.4 (dashed blue line) at the point E shown in Fig. 8 aj. The blue, black and red lines paralleled with Y axis refer to sea fog onset time in Exp-L0.4, Exp-L8 and Exp-L14, respectively.

deep. The biases of simulations continue to increase as z_1 becomes further lower.

Over sea, the experiment with $z_1 =$ 8 m performs best to reproduce the sea fog event in terms of both the onset time and the fog area. The sensitivity of simulated sea fog to z_1 can be attributed to the dependence of virtual potential temperature at z_1 [$\theta_v(z_1)$] on the value of z_1. In the present study, one important process is that relatively warm air mass passes over a cold sea surface and the near-surface air is cooled by the air-sea interaction through negative surface sensible heat flux. The heat capacity of the air mass in the lowest model layer is proportional to z_1, and z_1 dominates the variation rate of $\theta_v(z_1)$. Assuming the surface sensible heat flux remains the same in experiments with various z_1, air temperature of the lowest model level could respond more quickly (slowly) to the sensible heat flux if z_1 is lower (higher) because of a smaller (larger) heat capacity. Thus, a lower (higher) z_1 always causes a quicker (slower) decrease in $\theta_v(z_1)$ and subsequently leads to an earlier (later) sea fog formation. Compared to observed sea fog derived from the MTSAT data, z_1 below (above) 8 m leads to a too early (late) fog formation. After the initial sea fog formations at the lowest model level, vertical turbulent mixing transports warmer air from upper levels to the lowest model level and brings cooler air from the lowest model level to upper levels. This process limits the degree of $\theta_v(z_1)$ reduction and plays an important role for further evolution (either dissipating or extending) of the sea fog. With z_1 below 4 m, $\theta_v(z_1)$ responds too quickly to turbulent heating from the upper level, and this process dominates and leads to early dissipation of the sea fog. If $\theta_v(z_1)$ is not warm enough, the sea fog would redevelop with lower top height. With z_1 = 8 m, $\theta_v(z_1)$ responds moderately to turbulent mixing between model levels, and sea fog maintains at the lowest model level. As the temperature at the second model level decreases enough due to the turbulence cooling from the lowest model layer, sea fog starts to form at this level, which is shown as upward extension of the sea fog. At a certain stage after the initial sea fog formation, strong longwave radiative cooling of fog droplets becomes the dominant cooling process in the fog layer, which leads to the maintenance and further vertical development of the sea fog. Sea fog can maintain as above but develop later when z_1 gets above 8 m, since the higher z_1 means the slower decrease in the temperature at the second model level and less condensation of fog droplets.

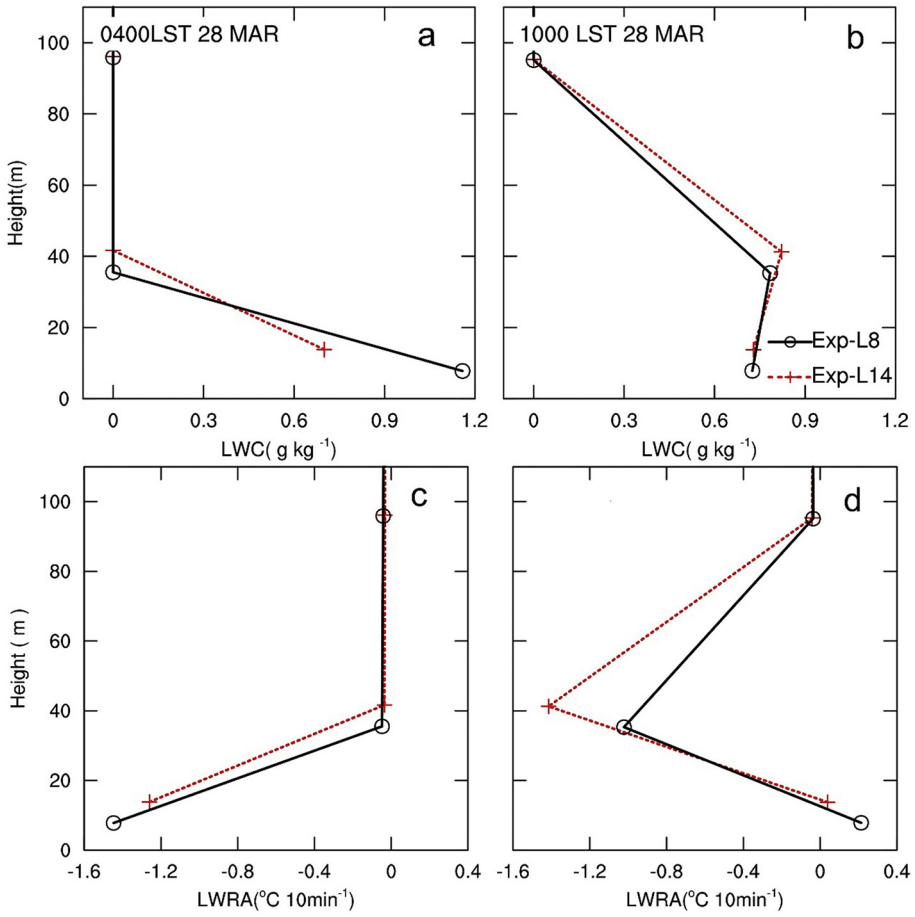

Fig. 12. Vertical profiles of (a, b) *LWC* and (c, d) virtual potential temperature tendency due to *RALW* in Exp-L14 (dotted red line) and Exp-L8 (solid black line) at the point E shown in Fig. 8 aj during (a, c) maintenance and (b, d) development stages of sea fog.

In summary, moderate z_1 is essential to reproduce the realistic onset time of sea fog and its area. A lower z_1 may lead to an earlier formation and smaller area of sea fog, while a higher z_1 would delay the formation and development of sea fog.

This study focuses on the significant role of the lowest model level in capturing sea fog process, particularly during the early stage when sea fog remains at low levels. Accurate simulation of the radiative cooling at the fog top may be critical for realistically reproducing the whole life cycle of the sea fog and capturing its fog-top height. This should require an appropriate vertical resolution together with a reasonable radiative cooling process near the fog top. Inspiring studies that take into account on the effects of turbulent mixing driven by radiative cooling atop the cloud and radiation fog by using modified YSU schemes have been published recently (Ghonima et al., 2017; Wilson and Fovell, 2018). Further numerical investigations will be necessary with focus on the role of vertical resolution near the sea fog top based on these modified YSU schemes.

Acknowledgements

This work was supported by the National Key Research and Development Program of China (2017YFC1404200, 2017YFC1404100) and the National Natural Science Foundation of China (41276009). We thank the China Scholarship Council for their financial support towards the first author. The second author was partially supported by the NOAA VORTEX-SE Program through grant NA17OAR4590188. Computations were performed at the San Diego Supercomputer Center (SDSC).

References

Aligo, E.A., Gallus Jr., W.A., Segal, M., 2009. On the impact of WRF model vertical grid resolution on Midwest summer rainfall forecasts. Weather Forecast. 24 (2), 575–594. https://doi.org/10.1175/2008WAF2007101.1.

Avolio, E., Federico, S., Miglietta, M.M., Feudo, T.L., Calidonna, C.R., Sempreviva, A.M., 2017. Sensitivity analysis of WRF model PBL schemes in simulating boundary-layer variables in southern Italy: an experimental campaign. Atmos. Res. 192, 58–71. https://doi.org/10.1016/j.atmosres.2017.04.003.

Bechtold, P., Krueger, S.K., Lewellen, W.S., Van Meijgaard, E., Moeng, C.H., Randall, D.A., Van Ulden, A., Wang, S., 1996. Modeling a stratocumulus-topped PBL: intercomparison among different one-dimensional codes and with large eddy simulation. Bull. Am. Meteorol. Soc. 77 (9), 2033–2042. https://doi.org/10.1175/1520-0477(1996)077<2033:MASTPI>2.0.CO;2.

Bergot, T., Guedalia, D., 1994. Numerical forecasting of radiation fog. Part I: numerical model and sensitivity tests. Mon. Weather Rev. 122 (6), 1218–1230. https://doi.org/10.1175/1520-0493(1994)122<1218:NFORFP>2.0.CO;2.

Bergot, T., Terradellas, E., Cuxart, J., Mira, A., Liechti, O., Mueller, M., Nielsen, N.W., 2007. Intercomparison of single-column numerical models for the prediction of radiation fog. J. Appl. Meteorol. Climatol. 46 (4), 504–521. https://doi.org/10.1175/JAM2475.1.

Borge, R., Alexandrov, V., Del Vas, J.J., Lumbreras, J., Rodriguez, E., 2008. A comprehensive sensitivity analysis of the WRF model for air quality applications over the Iberian Peninsula. Atmos. Environ. 42 (37), 8560–8574. https://doi.org/10.1016/j.atmosenv.2008.08.032.

Braun, S.A., Tao, W.K., 2000. Sensitivity of high-resolution simulations of hurricane Bob (1991) to planetary boundary layer parameterizations. Mon. Weather Rev. 128 (12), 3941–3961. https://doi.org/10.1175/1520-0493(2000)129<3941:SOHRSO>2.0.CO;2.

Chaouch, N., Temimi, M., Weston, M., Ghedira, H., 2017. Sensitivity of the meteorological model WRF-ARW to planetary boundary layer schemes during fog conditions in a coastal arid region. Atmos. Res. 187, 106–127. https://doi.org/10.1016/j.atmosres.2016.12.009.

Chen, F., Dudhia, J., 2001. Coupling an advanced land surface-hydrology model with the Penn State-NCAR MM5 modeling system. Part I: model implementation and Sensitivity. Mon. Weather Rev. 129 (4), 569–585. https://doi.org/10.1175/1520-0493(2001)129<0569:CAALSH>2.0.CO;2.

Cho, Y.-K., Kim, M.-O., Kim, B.-C., 2000. Sea fog around the Korean Peninsula. J. Appl. Meteorol. 39 (12), 2473–2479. https://doi.org/10.1175/1520-0450(2000)039<2473:SFATKP>2.0.CO;2.
Choi, H., Speer, M.S., 2006. The influence of synoptic-mesoscale winds and sea surface temperature distribution on fog formation near the Korean western Peninsula. Meteorol. Appl. 13 (4), 347–360. https://doi.org/10.1017/S1350482706002398.
Cohen, A.E., Cavallo, S.M., Coniglio, M.C., Brooks, H.E., 2015. A review of planetary boundary layer parameterization schemes and their sensitivity in simulating a Southeast U.S. cold season severe weather environments. Weather Forecast. 30 (3), 591–612. https://doi.org/10.1175/WAF-D-14-00105.1.
Coniglio, M.C., Correia, J., Marsh, P.T., Kong, F., 2013. Verification of convection-allowing WRF model forecasts of the planetary boundary layer using sounding observations. Weather Forecast. 28 (3), 842–862. https://doi.org/10.1175/WAF-D-12-00103.1.
Doswell III, C.A., Flueck, J.A., 1989. Forecasting and verifying in a field research project: DOPLIGHT'87. Weather Forecast. 4 (2), 97–109. https://doi.org/10.1175/1520-0434(1989)004<0097:FAVIAF>2.0.CO;2.
Douglas, C., 1930. Cold fogs over the sea. Meteorol. Mag. 65, 133–135.
Dudhia, J., 1989. Numerical study of convection observed during the Winter Monsoon Experiment using a mesoscale two-dimensional model. J. Atmos. Sci. 46 (20), 3077–3107. https://doi.org/10.1175/1520-0469(1989)046<3077:NSOCOD>2.0.CO;2.
Findlater, J., Roach, W.T., McHugh, B.C., 1989. The haar of north-east Scotland. Q. J. R. Meteorol. Soc. 115 (487), 581–608. https://doi.org/10.1002/qj.49711548709.
Foken, T., 2006. 50 years of the Monin-Obukhov similarity theory. Bound.-Layer Meteorol. 119 (3), 431–447. https://doi.org/10.1007/s10546-006-9048-6.
Fu, G., Guo, J., Xie, S.-P., Duan, Y., Zhang, M., 2006. Analysis and high-resolution modeling of a dense sea fog event over the Yellow Sea. Atmos. Res. 81 (4), 292–303. https://doi.org/10.1016/j.atmosres.2006.01.005.
Fu, G., Zhang, S., Gao, S., Li, P., 2012. Understanding of Sea Fog over the China Seas. Press, Beijing, China, China Meteorol.
Gao, S., Lin, H., Shen, B., Fu, G., 2007. A heavy sea fog event over the Yellow Sea in March 2005: Analysis and numerical modeling. Adv. Atmos. Sci. 24 (1), 65–81. https://doi.org/10.1007/s00376-007-0065-2.
Gao, S., Qi, Y., Zhang, S., Fu, G., 2010. Initial conditions improvement of sea fog numerical modeling over the Yellow Sea by using cycling 3DVAR. Part I: WRF numerical experiments (in Chinese). J. Ocean Univ. China 40 (10), 001–009.
García-Díez, M., Fernández, J., Fita, L., Yagüe, C., 2013. Seasonal dependence of WRF model biases and sensitivity to PBL schemes over Europe. Q. J. R. Meteorol. Soc. 139 (671), 501–514. https://doi.org/10.1002/qj.1976.
Ghonima, M.S., Yang, H., Kim, C.K., Heus, T., Kleissl, J., 2017. Evaluation of WRF SCM simulations of stratocumulus-topped marine and coastal boundary layers and improvements to turbulence and entrainment parameterizations. J. Adv. Model. Earth Syst. 9, 2635–2653. https://doi.org/10.1002/2017MS001092.
Gultepe, I., Tardif, R., Michaelides, S.C., Cermak, J., Bott, A., Bendix, J., Müller, M.D., Pagowski, M., Hansen, B., Ellrod, G., Jacobs, W., Toth, G., Cober, S.G., 2007. Fog research: a review of past achievements and future perspectives. Pure Appl. Geophys. 164, 1121–1159. https://doi.org/10.1007/978-3-7643-8419-7_3.
Han, Z., Ueda, H., An, J., 2008. Evaluation and intercomparison of meteorological predictions by five MM5-PBL parameterizations in combination with three land-surface models. Atmos. Environ. 42 (2), 233–249. https://doi.org/10.1016/j.atmosenv.2007.09.053.
Hariprasad, K.B.R.R., Srinivas, C.V., Singh, A.B., Rao, S.V.B., Baskaran, R., Venkatraman, B., 2014. Numerical simulation and intercomparison of boundary layer structure with different PBL schemes in WRF using experimental observations at a tropical site. Atmos. Res. 145, 27–44. https://doi.org/10.1016/j.atmosres.2014.03.023.
Hennemuth, B., Lammert, A., 2006. Determination of the atmospheric boundary layer height from radiosonde and lidar backscatter. Bound.-Layer Meteorol. 120 (1), 181-200. https://doi.org/10.1007/s10546-005-9035-3.
Heo, K.-Y., Ha, K.-J., Mahrt, L., Shim, J.S., 2010. Comparison of advection and steam fogs: from direct observation over the sea. Atmos. Res. 98 (2), 426–437. https://doi.org/10.1016/j.atmosres.2010.08.004.
Hong, S.-Y., 2010. A new stable boundary-layer mixing scheme and its impact on the simulated East Asia summer monsoon. Q. J. R. Meteorol. Soc. 136 (651), 1481–1496. https://doi.org/10.1002/qj.665.
Hong, S.-Y., Noh, Y., Dudhia, J., 2006. A new vertical diffusion package with an explicit treatment of entrainment processes. Mon. Weather Rev. 134 (9), 2318–2341. https://doi.org/10.1175/MWR3199.1.
Hu, X.-M., Xue, M., 2016. Influence of synoptic sea-breeze fronts on the urban heat island intensity in Dallas–Fort Worth. Texas. Mon. Weather Rev. 144 (4), 1487–1507. https://doi.org/10.1175/MWR-D-15-0201.1.
Hu, X.-M., Nielsen-Gammon, J.W., Zhang, F., 2010. Evaluation of three planetary boundary layer schemes in the WRF model. J. Appl. Meteorol. Climatol. 49 (9), 1831–1844. https://doi.org/10.1175/2010JAMC2432.1.
Hu, X.-M., Klein, P.M., Xue, M., 2013. Evaluation of the updated YSU planetary boundary layer scheme within WRF for wind resource and air quality assessments. J. Geophys. Res. Atmos. 118 (18), 10490–10505. https://doi.org/10.1002/jgrd.50823.
Huang, H.-Y., Hall, A., Teixeira, J., 2013. Evaluation of the WRF PBL parameterizations for marine boundary layer clouds: cumulus and stratocumulus. Mon. Weather Rev. 141 (7), 2265–2271. https://doi.org/10.1175/MWR-D-12-00292.1.
Iacono, M.J., Delamere, J.S., Mlawer, E.J., Shephard, M.W., Clough, S.A., Collins, W.D., 2008. Radiative forcing by long-lived greenhouse gases: calculations with the AER radiative transfer models. J. Geophys. Res. Atmos. 113, D13103. https://doi.org/10.1029/2008JD009944.
Jankov, I., Gallus, W.A., Segal, M., Shaw, B., Koch, S.E., 2005. The impact of different WRF model physical parameterizations and their interactions on warm season MCS rainfall. Weather Forecast. 20 (6), 1048–1060. https://doi.org/10.1175/WAF888.1.
Jankov, I., Schultz, P.J., Anderson, C.J., Koch, S.E., 2007. The impact of different physical parameterizations and their interactions on cold season QPF in the American river basin. J. Hydrometeorol. 8 (5), 1141–1151. https://doi.org/10.1175/JHM630.1.
Jiménez, P.A., Dudhia, J., González-Rouco, J.F., Navarro, J., Montávez, J.P., García-Bustamante, E., 2012. A revised scheme for the WRF surface layer formulation. Mon. Weather Rev. 140 (3), 898–918. https://doi.org/10.1175/MWR-D-11-00056.1.
Kain, J.S., 2004. The Kain–Fritsch convective parameterization: an update. J. Appl. Meteorol. 43 (1), 170–181. https://doi.org/10.1175/1520-0450(2004)043<0170:TKCPAU>2.0.CO;2.
Kain, J.S., Fritsch, J.M., 1990. A one-dimensional entraining/detraining plume model and its application in convective parameterization. J. Atmos. Sci. 47 (23), 2784–2802. https://doi.org/10.1175/1520-0469(1990)047<2784:AODEPM>2.0.CO;2.
Khain, A., Lynn, B., Shpund, J., 2016. High resolution WRF simulations of Hurricane Irene: sensitivity to aerosols and choice of microphysical schemes. Atmos. Res. 167, 129–145. https://doi.org/10.1016/j.atmosres.2015.07.014.
Kim, C.K., Yum, S.S., 2010. Local meteorological and synoptic characteristics of fogs formed over Incheon international airport in the west coast of Korea. Adv. Atmos. Sci. 27 (4), 761–776. https://doi.org/10.1007/s00376-009-9090-7.
Kim, C.K., Yum, S.S., 2012. A numerical study of sea-fog formation over cold sea surface using a one-dimensional turbulence model coupled with the Weather Research and Forecasting model. Bound.-Layer Meteorol. 143 (3), 481–505. https://doi.org/10.1007/s10546-012-9706-9.
Kimball, S.K., Dougherty, F.C., 2006. The sensitivity of idealized hurricane structure and development to the distribution of vertical levels in MM5. Mon. Weather Rev. 134 (7), 1987–2008. https://doi.org/10.1175/MWR3171.1.
Kong, F., 2002. An experimental simulation of a coastal fog-stratus case using COAMPS (tm) model. Atmos. Res. 64 (1), 205–215. https://doi.org/10.1016/S0169-8095(02)00092-3.
Koračin, D., Dorman, C.E., 2017. Marine fog: Challenges and Advancements in Observations, Modeling, and Forecasting. Springer International Publishing, San Diego, CA, USA. https://doi.org/10.1007/978-3-319-45229-6.
Koračin, D., Lewis, J., Thompson, W.T., Dorman, C.E., Businger, J.A., 2001. Transition of stratus into fog along the California coast: observations and modeling. J. Atmos. Sci. 58 (13), 1714–1731. https://doi.org/10.1175/1520-0469(2001)058<1714:TOSIFA>2.0.CO;2.
Koračin, D., Businger, J.A., Dorman, C.E., Lewis, J.M., 2005a. Formation, evolution, and dissipation of coastal sea fog. Bound.-Layer Meteorol. 117 (3), 447–478. https://doi.org/10.1007/s10546-005-2772-5.
Koračin, D., Leipper, D.F., Lewis, J.M., 2005b. Modeling sea fog on the U.S. California coast during a hot spell event. Geofizika 22, 59–82.
Koračin, D., Dorman, C.E., Lewis, J.M., Hudson, J.G., Wilcox, E.M., Torregrosa, A., 2014. Marine fog: a review. Atmos. Res. 143, 142–175. https://doi.org/10.1016/j.atmosres.2013.12.012.
Lamb, H., 1943. Haars or North Sea fogs on the coasts of Great Britain. Meteorology Office Publication M.O. 504, 24.
Lemone, M.A., Tewari, M., Chen, F., Dudhia, J., 2013. Objectively determined fair-weather CBL depths in the ARW-WRF model and their comparison to cases-97 observations. Mon. Weather Rev. 141 (1), 30–54. https://doi.org/10.1175/MWR-D-12-00106.1.
Lewis, J.M., Koračin, D., Redmond, K.T., 2004. Sea fog research in the United Kingdom and United States: a historical essay including outlook. Bull. Am. Meteorol. Soc. 85 (3), 395–408. https://doi.org/10.1175/BAMS-85-3-395.
Li, X., Pu, Z., 2008. Sensitivity of numerical simulation of early rapid intensification of hurricane Emily (2005) to cloud microphysical and planetary boundary layer parameterizations. Mon. Weather Rev. 136 (12), 4819–4838. https://doi.org/10.1175/2008MWR2366.1.
Lin, Y.-L., Farley, R.D., Orville, H.D., 1983. Bulk parameterization of the snow field in a cloud model. J. Clim. Appl. Meteorol. 22 (6), 1065–1092. https://doi.org/10.1175/1520-0450(1983)022<1065:BPOTSF>2.0.CO;2.
Liu, J., Xie, S.-P., Norris, J.R., Zhang, S., 2014. Low-level cloud response to the Gulf Stream front in winter using CALIPSO. J. Clim. 27 (12), 4421–4432. https://doi.org/10.1175/JCLI-D-13-00469.1.
Lu, X., Gao, S., Rao, L., Wang, Y., 2014. Sensitivity study of WRF parametrization schemes for the spring sea fog in the Yellow Sea (in Chinese). J. Appl. Meteorol. Sci. 25 (3), 312–320.
Ma, Z., Fei, J., Huang, X., Cheng, X., 2014. Impacts of the lowest model level height on tropical cyclone intensity and structure. Adv. Atmos. Sci. 31 (2), 421–434. https://doi.org/10.1007/s00376-013-3044-9.
Minnis, P., Yost, C.R., Sun-Mack, S., Chen, Y., 2008. Estimating the top altitude of optically thick ice clouds from thermal infrared satellite observations using CALIPSO data. Geophys. Res. Lett. 35 (12), L12801. https://doi.org/10.1029/2008GL033947.
Monin, A.S., Obukhov, A.M., 1954. Basic turbulence mixing laws in the atmospheric surface layer. Tr. Akad. Nauk SSSR Geofiz. Inst 24, 163–187.
Nakanishi, M., Niino, H., 2006. An improved Mellor–Yamada level 3 model: its numerical stability and application to a regional prediction of advection fog. Bound.-Layer Meteorol. 119 (2), 397–407. https://doi.org/10.1007/s10546-005-9030-8.
Nakanishi, M., Niino, H., 2009. Development of an improved turbulence closure model for the atmospheric boundary layer. J. Meteorol. Soc. Jpn. Ser. II 87 (5), 895–912. https://doi.org/10.2151/jmsj.87.895.
Nielsen-Gammon, J.W., Powell, C.L., Mahoney, M.J., Angevine, W.M., Senff, C., White, A., Berkowitz, C., Doran, C., Knupp, K., 2008. Multisensor estimation of mixing heights over a coastal city. J. Appl. Meteorol. Climatol. 47 (1), 27–43. https://doi.org/10.1175/2007JAMC1503.1.
Noh, Y., Cheon, W.G., Hong, S.-Y., Raasch, S., 2003. Improvement of the K-profile model for the planetary boundary layer based on large eddy simulation data. Bound.-Layer

Meteorol. 107 (2), 401–427. https://doi.org/10.1023/A:1022146015946.
Nolan, D.S., Zhang, J.A., Stern, D.P., 2009. Evaluation of planetary boundary layer parameterizations in tropical cyclones by comparison of in situ observations and high-resolution simulations of hurricane Isabel (2003). Part I: initialization, maximum winds, and the outer-core boundary layer. Mon. Weather Rev. 137 (11), 3651–3674. https://doi.org/10.1175/2009MWR2785.1.
Oliver, D.A., Lewellen, W.S., Williamson, G.G., 1978. The interaction between turbulent and radiative transport in the development of fog and low-level stratus. J. Atmos. Sci. 35 (2), 301–316.
Pagowski, M., Gultepe, I., King, P., 2004. Analysis and modeling of an extremely dense fog event in southern Ontario. J. Appl. Meteorol. 43 (1), 3–16. https://doi.org/10.1175/1520-0450(2004)043<0003:AAMOAE>2.0.CO;2.
Román-Cascón, C., Yagüe, C., Sastre, M., Maqueda, G., Salamanca, F., Viana, S., 2012. Observations and WRF simulations of fog events at the Spanish Northern Plateau. Adv. Sci. Res. 8 (1), 11–18. https://doi.org/10.5194/asr-8-11-2012.
Shin, H.H., Hong, S.-Y., 2011. Intercomparison of planetary boundary-layer parametrizations in the WRF model for a single day from CASES-99. Bound.-Layer Meteorol. 139 (2), 261–281. https://doi.org/10.1007/s10546-010-9583-z.
Shin, H.H., Hong, S.-Y., Dudhia, J., 2012. Impacts of the lowest model level height on the performance of planetary boundary parameterizations. Mon. Weather Rev. 140 (2), 664–682. https://doi.org/10.1175/MWR-D-11-00027.1.
Skamarock, W.C., Klemp, J.B., Dudhia, J., Gill, D.O., Barker, D.M., Duda, M.G., Huang, X.-Y., Wang, W., Powers, J.G., 2008. A description of the advanced research WRF version 3. NCAR Technical Note, NCAR, Boulder, Colorado.
Steeneveld, G.J., Ronda, R.J., Holtslag, A.A.M., 2015. The challenge of forecasting the onset and development of radiation fog using mesoscale atmospheric models. Bound.-Layer Meteorol. 154 (2), 265–289. https://doi.org/10.1007/s10546-014-9973-8.
Stein, T.H.M., Parker, D.J., Delanoë, J., Dixon, N.S., Hogan, R.J., Knippertz, P., Maidment, R.I., Marsham, J.H., 2011. The vertical cloud structure of the West African monsoon: a 4 year climatology using CloudSat and CALIPSO. J. Geophys. Res. Atmos. 116, D22205. https://doi.org/10.1029/2011JD016029.
Stensrud, D.J., 2007. Parameterization Schemes: Keys to Understanding Numerical Weather Prediction Models. Cambridge University Press, New York, USA.
Stull, R.B., 1988. An Introduction to Boundary Layer Meteorology. Kluwer Academic Publishers, Hingham, MA, USA.
Subrahamanyam, D.B., Anurose, T.J., Kumar, N.K., Mohan, M., Kunhikrishnan, P.K., John, S.R., Prijith, S.S., Dutt, C.B.S., 2012. Spatial and temporal variabilities in vertical structure of the Marine Atmospheric Boundary Layer over Bay of Bengal during Winter Phase of Integrated Campaign for Aerosols, gases and Radiation Budget. Atmos. Res. 107, 178–185. https://doi.org/10.1016/j.atmosres.2011.12.014.
Tardif, R., 2007. The impact of vertical resolution in the explicit numerical forecasting of radiation fog: a case study. Pure Appl. Geophys. 164 (6), 1221–1240. https://doi.org/10.1007/s00024-007-0216-5.
Taylor, G.I., 1917. The formation of fog and mist. Q. J. R. Meteorol. Soc. 43 (183), 241–268. https://doi.org/10.1002/qj.49704318302.
Teixeira, J.C., Carvalho, A.C., Tuccella, P., Curci, G., Rocha, A., 2016. WRF-chem sensitivity to vertical resolution during a saharan dust event. Phys. Chem. Earth Parts A/B/C 94, 188–195. https://doi.org/10.1016/j.pce.2015.04.002.
Trémant, M., 1987. La prèvision du brouilliard en mer. Météorologie Maritime et Activities, Océanographique Connexes Paport, Vol. 20, WMO, Geneva, Switzerland.
Van der Velde, I.R., Steeneveld, G.J., Wichers Schreur, B.G.J., Holstlag, A.A.M., 2010. Modeling and forecasting the onset and duration of severe radiation fog under frost conditions. Mon. Weather Rev. 138 (11), 4237–4253. https://doi.org/10.1175/2010MWR3427.1.
Wang, B.H., 1985. Sea Fog. Springer-Verlag, New York, USA.
Wang, Y., Gao, S., 2016. Assimilation of Doppler Radar radial velocity in Yellow Sea fog numerical modeling (in Chinese). J. Ocean Univ. China 46 (8), 1–12. https://doi.org/10.16441/j.cnki.hdxb.20150361.
Wang, Y., Gao, S., Fu, G., Sun, J., Zhang, S., 2014. Assimilating MTSAT-derived humidity in nowcasting sea fog over the Yellow Sea. Weather Forecast. 29 (2), 205–225. https://doi.org/10.1175/WAF-D-12-00123.
Wei, H., Segal, M., Gutowski, W.J., Pan, Z., Arritt, R.W., Gallus, W.A., 2001. Sensitivity of simulated regional surface thermal fluxes during warm advection snowmelt to selection of the lowest model layer height. J. Hydrometeorol. 2 (4), 395–405. https://doi.org/10.1175/1525-7541(2001)002<0395:SOSRST>2.0.CO;2.
Wilson, T.H., Fovell, R.G., 2016. Modeling the evolution and life cycle of stable cold pools. Weather Forecast. 31 (6), 1753–1769. https://doi.org/10.1175/WAF-D-16-0108.1.
Wilson, T.H., Fovell, R.G., 2018. Modeling the evolution and life cycle of radiative cold pools and fog. Weather Forecast. 33 (1), 203–220. https://doi.org/10.1175/WAF-D-17-0109.1.
Yang, Y., Gao, S., 2015. Analysis on the synoptic characteristics and inversion layer formation of the Yellow Sea Fogs (in Chinese). J. Ocean Univ. China 45 (6), 19–30. https://doi.org/10.16441/j.cnki.hdxb.20140059.
Yang, Y., Gao, S., 2016. Sensitivity study of vertical resolution in WRF numerical simulation for sea fog over the Yellow Sea (in Chinese). Acta Meteorol. Sin. 74 (6), 974–988. https://doi.org/10.11676/qxxb2016.062.
Yi, L., Zhang, S.P., Thies, B., Shi, X.M., Trachte, K., Bendix, J., 2015. Spatio-temporal detection of fog and low stratus top heights over the Yellow Sea with geostationary satellite data as a precondition for ground fog detection—a feasibility study. Atmos. Res. 151, 212–223. https://doi.org/10.1016/j.atmosres.2014.03.020.
Zängl, G., Gohm, A., Obleitner, F., 2008. The impact of the PBL scheme and the vertical distribution of model layers on simulations of Alpine foehn. Meteorol. Atmos. Phys. 99 (1), 105–128. https://doi.org/10.1007/s00703-007-0276-1.
Zhang, S., 2012. Recent observations and modeling study about sea fog over the Yellow Sea and East China Sea. J. Ocean Univ. China 11 (4), 465–472. https://doi.org/10.1007/s11802-012-1873-2.
Zhang, D., Anthes, R.A., 1982. A high-resolution model of the planetary boundary layer—Sensitivity tests and comparisons with SESAME-79 data. J. Appl. Meteorol. 21 (11), 1594–1609. https://doi.org/10.1175/1520-0450(1982)021<1594:AHRMOT>2.0.CO;2.
Zhang, F., Pu, Z., 2017. Sensitivity of numerical simulations of an ice fog event to PBL and surface layer parameterization schemes with WRF model. In: 97th American Meteorological Society Annual Meeting. WA, USA, Seattle.
Zhang, S., Ren, Z., 2010. The influence of the thermal effect of underlaying surface on the spring sea fog over the Yellow Sea: Observations and numerical simulations (in Chinese). Acta Meteorol. Sin. 68 (4), 439–449. https://doi.org/10.11676/qxxb2010.043.
Zhang, D., Wang, X., 2003. Dependence of hurricane intensity and structures on vertical resolution and time-step size. Adv. Atmos. Sci. 20 (5), 711–725. https://doi.org/10.1007/BF02915397.
Zhang, S., Ren, Z., Liu, J., Yang, Y., Wang, X., 2008. Variation in the lower level of the PBL associated with the Yellow Sea fog—new observations by L-Band Radar. J. Ocean Univ. China 7 (4), 353–361. https://doi.org/10.1007/s11802-008-0353-1.
Zhang, S., Xie, S.-P., Liu, Q., Yang, Y., Wang, X., Ren, Z., 2009. Seasonal variations of Yellow Sea fog: observations and mechanisms. J. Clim. 22 (24), 6758–6772. https://doi.org/10.1175/2009JCLI2806.1.
Zhang, S., Chen, Y., Long, J., Han, G., 2015. Interannual variability of sea fog frequency in the Northwestern Pacific in July. Atmos. Res. 151, 189–199. https://doi.org/10.1016/j.atmosres.2014.04.004.
Zhou, B., Du, J., 2010. Fog prediction from a multimodel mesoscale ensemble prediction system. Weather Forecast. 25 (1), 303–322. https://doi.org/10.1175/2009WAF2222289.1.
Zhou, B., Du, J., Gultepe, I., Dimego, G., 2011. Forecast of low visibility and fog from NCEP: current status and efforts. Pure Appl. Geophys. 169 (5), 895–909. https://doi.org/10.1007/s00024-011-0327-x.